The Impact of a Nickel-Chromium Buffer Layer on the Magnetoresistance of Permalloy

by

Matthew J. Farinelli

B.E. Engineering Science
State University of New York at Stony Brook, 1996

SUBMITTED TO THE DEPARTMENT OF MATERIALS SCIENCE & ENGINEERING IN PARTIAL FULFILLMENT OF THE REQUIREMENTS FOR THE DEGREE OF

MASTER OF SCIENCE IN MATERIALS SCIENCE & ENGINEERING
AT THE
MASSACHUSETTS INSTITUTE OF TECHNOLOGY

JUNE 1999

Signature of Author.....
Department of Materials Science & Engineering
May 7, 1999

Certified by .....
Robert C. O'Handley
Senior Research Associate
Thesis Advisor

.....
Samuel M. Allen
Professor of Materials Science & Engineering
Thesis Co-Advisor

Accepted by .....
Linn W. Hobbs
John F. Elliot Professor of Materials
Chairman, Departmental Committee on Graduate Students

The Impact of a Nickel-Chromium Buffer Layer on the Magnetoresistance of Permalloy

by

Matthew J. Farinelli

Submitted to the Department of Materials Science & Engineering on May 7, 1999 in Partial Fulfillment of the Requirements for the Degree of Master of Science in Materials Science & Engineering

ABSTRACT

An experimental study was performed to determine the impact of a nickel-chromium seed layer on the magnetoresistive properties of Permalloy ($Ni_{81}Fe_{19}$). Samples were fabricated using a custom-built DC magnetron sputtering system equipped with a specially designed, *in-situ* four-point magnetoresistance probe. Unpatterned metallic multilayer thin film samples of the form $Ni_{80}Cr_{20}$(50Å)/$Ni_{81}Fe_{19}$(200Å)/$Ni_{80}Cr_{20}$(50Å) were deposited onto amorphous silica (SiO_2) substrates. A post deposition annealing treatment of the 50Å $Ni_{80}Cr_{20}$ seed layer at a temperature of 200°C was performed for various times prior to the deposition of the magnetoresistive Permalloy layer and the $Ni_{80}Cr_{20}$ capping layer. This heat treatment process resulted in a generally improved maximum magnetoresistance ratio of the Permalloy layer. However, this system showed a maximum magnetoresistance ratio of ~1%, which is 70% lower than that expected for thin film Permalloy. This lower than average value was attributed to an increased resistivity in the Permalloy layer (~70μΩ-cm). Chromium diffusion into the Permalloy layer is postulated as the cause for this increase. SEM micrographs confirmed an improvement in the surface morphology (surface roughness and pinhole density) of the heat-treated samples. Higher surface mobility of adatoms is postulated as the mechanism for improved surface morphology. This improvement in film quality correlates to the improved magnetoresistive properties of the multilayer samples.

Thesis Supervisor: Robert C. O'Handley

Title: Senior Research Associate

Table of Contents

List of Figures

List of Tables

Acknowledgments

I would first like to thank my God for His creation, His unfailing love, and His support during my life. It is through Him that all things are possible.
I want to especially thank my wife, Christine, for her unwavering love during this time in our marriage. Her constant support and love is what enabled me to persevere. I thank my father, Paul Sr., for being a role model in my life and for teaching me the value of a good education. Thanks and praise also go to my mother, Linda, for being so instrumental in my development.
I would like to also thank my advisor, Dr. Robert C. O'Handley, for his intellectual insights, caring personality, and constant enthusiasm. He has been a great source of motivation to me and I will always remember my three years as his student.
Finally I would like to acknowledge the financial support of the Department of Defense through its National Defense Science & Engineering Graduate (NDSEG) Research Fellowship and Applied Magnetics Corporation for its initial investment in this project.

This work made use of a MRSEC Shared Facilities supported by the National Science Foundation under Award #DMR-9400334

CHAPTER 1: INTRODUCTION

Information and knowledge are the key ingredients to profit and progress in today's society. Therefore, it is absolutely necessary to be able to access large quantities of information as rapidly as possible and to be able to take advantage of the vast knowledge base that exists in our society. Consequently, there is also a need for new and improved methods of data storage and retrieval.

Enter magnetism and magnetic materials. While the phenomenon of this 'sticky force' has been felt for millennia, it has only recently begun to show promise as a new candidate for information storage. In a mere fifty years, these materials and devices went from filling refrigerator-sized cabinets to inhabiting palm-sized digital cameras. Magnetoelectronics will soon become one of the fastest growing technological industries in our country. Dr. Gary Prinz, a leader in the field of magnetic materials, outlined some of the salient features of this new industry in his *Science* magazine article[1]. A key point

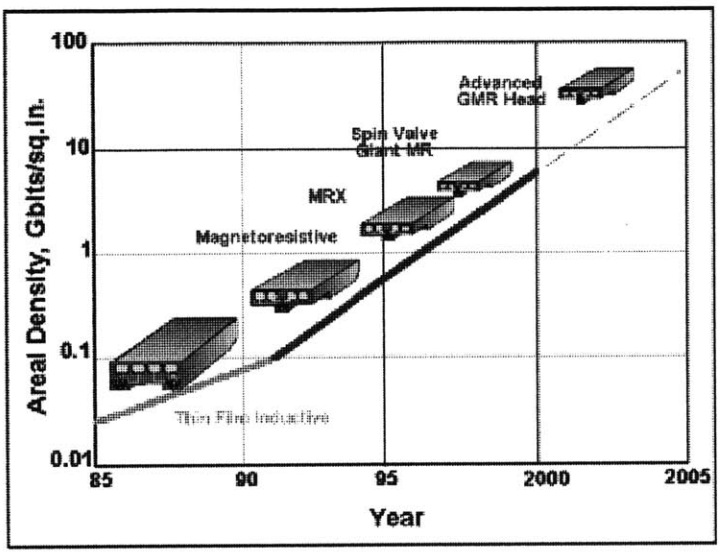

Figure 1.1: Evolution of MR heads with areal density of media. (*Courtesy of IBM Corporation*)

made in this review is that further development of giant magnetoresistive (GMR) technology can radically alter the microelectronic DRAM industry (a 100 billion-dollar per year industry). Dr. Prinz argues that spin-polarized electronics will offer us cheaper and faster technology if development can continue "as rapidly as the development of GMR read heads [in the magnetic recording industry]". The operative word is "if."

What drives this development, and ultimately limits it, is the principle of scaling. In order to increase the performance and commercial viability of thin film technology, manufacturers must continually shrink critical device features to increase device density and boost performance. Figure 1.1 shows a graph of IBM's recording head capabilities as a function of time. It is obvious from this graph that the trend is to shrink the size of components so as to achieve read-out for higher areal density media.

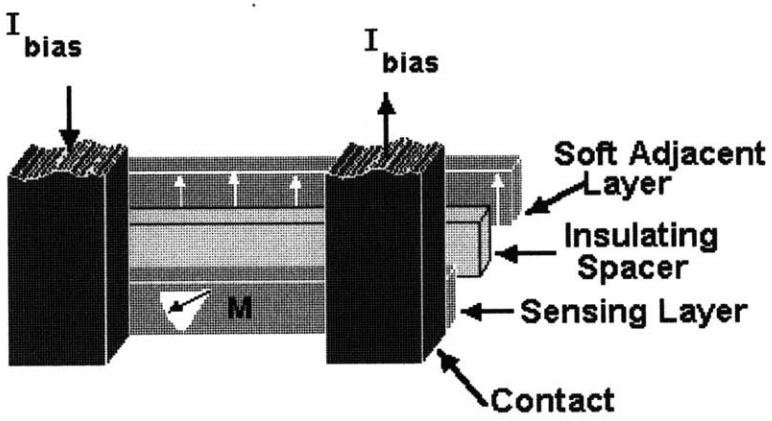

Figure 1.2: Schematic of an AMR sensor. (*Courtesy of IBM Corporation*)

For the most part, today's commercial magnetoelectronic devices come in the form of magnetoresistive (MR) sensors. Figure 1.2 shows a simple diagram of a magnetoresistive element. Like most other devices, MR sensors are being scaled also. These MR sensors are used in hard and floppy disk drives as read elements. Anisotropic magnetoresistance (AMR) sensors are found mainly in floppy drives and low-performance external drives, whereas, giant magnetoresistive (GMR) sensors are mainly used in high performance hard drives. While a typical AMR sensor will have an active magnetic element that is on the order of 100Å thick and 1μm x 2μm square, GMR sensors have active magnetic layers that are typically 50Å in thickness.

In a review article of devices fabricated for magnetic recording, Fontana *et al.* worked out the effects of dimensional variations in spin-valve devices on the output signal[2]. They find that in order to control the maximum magnetoresistive ratio (a critical device parameter) to within 10%, the magnetic sensing layer must have less than a 33% variation in its thickness. However, structural variations are not the whole story. The

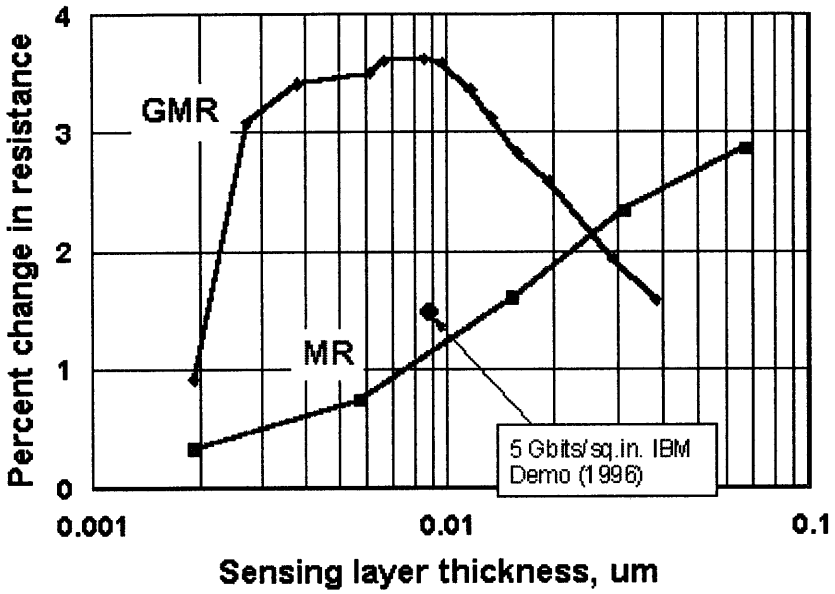

Figure 1.3: Change in resistance versus active layer thickness in a Co-based GMR spin-valve and an AMR sensor. ***(Courtesy of IBM Corporation)***

authors ignore the effects of chemical mixing, diffuse interfaces, and other process variations that can cause serious performance problems in these devices.

1.1 Motivation

In October of 1997, Applied Magnetics Corporation, a manufacturer of magnetoresistive (MR) sensors approached our group for help in designing thinner AMR elements to be used in magnetic storage devices. The initial effort was to look at the structural and chemical properties of the interfaces in these AMR elements and give feedback on any problems found. This exposure to a critical industrial need showed us that we could make a significant contribution in the area of MR head materials. So after this initial collaboration ended, interest in this problem remained, which grew into

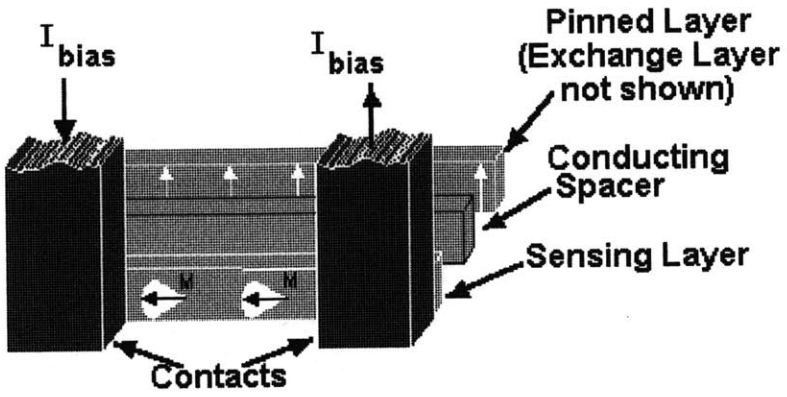

Figure 1.4: Simplified view of a GMR spin-valve. ***(Courtesy of IBM Corporation)***

investigating possible material substitutions in these devices to aid in decreasing device dimensions while maintaining or improving performance.

It soon became apparent that the magnetic recording industry would have to continue to scale down the size of active sensor components in order to keep up with the demand for greater data storage densities. Figure 1.3 on the previous page shows how the MR ratio (to be defined later) changes with element thickness in the two types of read heads, an AMR sensor and a GMR spin-vale sensor.

AMR sensors were proposed[6] as early as 1975 but did not come into commercial use until the mid-90's when thin film inductive sensors (those magnetic sensors based on Faraday's Law of induction) could no longer deliver the necessary performance needed by high-density media. AMR sensors change their resistance as the angle between the magnetization of the active layer and current direction changes. They follow a $\Delta R/R \propto cos^2 \theta_m$ empirical relationship (θ_m denotes the angle made between the

magnetization and the current directions). Figure 1.3 shows that the output of this sensor will decrease monotonically with decreasing element thickness. The reason for this is that AMR is a bulk scattering process. Therefore, as thickness decreases, $\Delta\rho$ decreases and ρ increases. Active layer thickness is critical to device performance thus care must be taken in designing the materials that surround this element. Most AMR sensors used in floppy drives today are designed with tantalum spacers and capping layers. As will be seen shortly, tantalum causes significant performance problems when active elements are reduced below 200Å (0.02 μm).

GMR spin-valve sensors became commercially important in the mid-1990's when IBM showed that they could be reliably fabricated using sputter deposition[7,8]. These sensors perform well in storage systems having data densities in the range of 5-10 Gbits/in^2 and are now well established in the commercial hard drive industry. GMR sensors are bi-layers of two ferromagnetic materials separated by a thin, non-magnetic spacer (usually copper or gold). One layer, referred to as the pinned layer, has its magnetization fixed in one direction. The magnetization of the second ferromagnetic layer, denoted as the free layer, can rotate by application of an external field, such as the fringe field of the magnetic domains on a hard disk. As electrons pass through this GMR device, their scattering rates in each layer depend upon the relative orientation of the magnetization directions. The resistivity of this device now depends on the relative orientation of the free layer and pinned layer magnetization vectors. The GMR sensor shows a peak in $\Delta\rho/\rho$ at some critical thickness. The reason for this is that the GMR

effect relies on the transport of carriers between the sensing layer and the pinned layer (see figure 1.4). Thus it shows a *1/t* dependence down to a certain thickness, *t**, below which ρ increases and film quality degrades. Hence $(\Delta\rho/\rho)_{GMR}$ vanishes near zero thickness. An important point in the design of these devices is that the spacer layer thickness is as critical in determining the maximum MR change as is the free layer thickness[9]. Therefore, care must be taken during processing in order to produce a working device.

Several previous studies of magnetic multi-layered systems have made it apparent that current MR materials used in industry can not keep up with scaling[3,4,5]. Industrial MR sensors are composed mainly of layered ferromagnetic and non-magnetic metals. A typical active element in an AMR sensor will consist of a tri-layer of β-Ta/NiFe/β-Ta. The aforementioned studies concluded that β-Ta (a metastable phase of bcc Ta) easily infiltrated the NiFe layer at low temperatures thereby degrading its magnetic moment and magnetoresistance. Low temperature diffusion in metals mainly occurs via grain boundary diffusion, assuming that the grain boundary diffusivity is greater than the bulk diffusivity.

The scope of this thesis research is to design and build a vacuum system capable of sputtering ferromagnetic multi-layers and to investigate the impact of a new non-magnetic spacer/seed layer on the magnetoresistive properties of Permalloy ($Ni_{81}Fe_{19}$). The non-magnetic seed layer was chosen to be a nickel-chromium alloy of composition $Ni_{80}Cr_{20}$. Reasons for this substitution will be given in Chapter 2.

In order to investigate how the non-magnetic seed layer affects the magnetoresistive layer, the saturation moment (M_s), the coercivity field (H_c), the anisotropy field (H_k), and the magnetoresistance ($\Delta\rho/\rho$) must be measured for samples prepared under various processing conditions, including deposition temperature and seed layer annealing times. The first three quantities can be easily measured in a vibrating sample magnetometer (VSM) but the latter needs to be measured by a specially modified four-point probe.

While the main focus of this research is to study the impact of new materials on AMR properties, the results are by no means limited to AMR devices. The techniques and procedures used in the fabrication of these materials can be easily adapted to the production of GMR structures. GMR and AMR devices, as well as spin-tunnel junctions and other spin-polarized electronics, suffer from the same problems. All of these structures rely on the fact that their metallic layers will remain intact. The conclusions of this thesis are equally valid for most magnetoelectronic devices.

1.2 Outline of Thesis

Chapter 1 of this thesis started off with a brief introduction to the topic of magnetoresistive sensors and a motivation for the research. The rest of this thesis is broken into four more chapters. Chapter 2 will cover some theoretical background to anisotropic magnetoresistance (AMR), its phenomenology, and its application to the design of magnetic sensors. The chapter will focus mainly on how important magnetic quantities, such as coercivity (H_c) and magnetic anisotropy (H_k), affect the output

response of a magnetoresistive multilayer. Finally, a link will be made between these important magnetic quantities and sample deposition parameters. Chapter 3 will introduce and explain the experimental techniques used in fabricating and characterizing these MR samples. Chapter 4 contains the results and observations of the experiments performed. Finally, the thesis ends with a discussion of the results, conclusions about this work and possible future directions.

CHAPTER 2: BACKGROUND

This chapter will briefly review the theory of anisotropic magnetoresistance (AMR) as it pertains to 3-d ferromagnetic transition metals and their alloys. The first section will attempt to qualitatively describe the microscopic basis for AMR using semiclassical and quantum physics. The spin-orbit interaction is the mechanism that leads to the AMR effect. However, no satisfactory microscopic model of AMR can be found in the literature that is both simple in its form and incorporates this interaction. Therefore, a brief description of what the spin-orbit energy is and how this interaction affects electron transport will be given.

Section 2 of this chapter covers the phenomenological aspects of AMR with respect to macroscopic variables such applied field (H), magnetic anisotropy (K_u), magnetization (**M**), and current direction (**j**). This section will lay the basis for the design

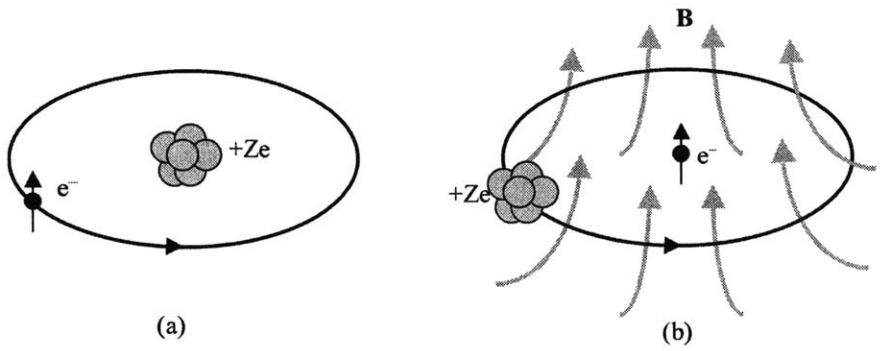

Figure 2.1: A simple view of an atom. (a) In the nuclear rest-frame, an electron with a spin of ±1/2 occupies an energy orbital. (b) From the electron's rest-frame, it appears as though a charge of +*Ze* moves around it, creating a B-field. Figure (b) shows how the orbital motion of the electron can couple to its spin.

of sensors using the AMR effect and discuss what variables are important in the fabrication of such sensors.

Section 3 will look at an actual sensor design and the processing techniques used in the construction of field sensors. Here we will discuss what thin film properties are important to the successful operation of such multilayers. This discussion will be important to chapters 3 and 4 where actual experimental data will be presented.

2.1 Microscopic Theory of Anisotropic Magnetoresistance

2.1.1:The spin-orbit interaction

William Thomson[10], honored as Lord Kelvin, first made the discovery of AMR in 1857. However, a microscopic theory of this effect did not appear for about a century. In the late 1940's and 1950's, Snoeck[11], Smit[12], and van Elst[13] noticed and studied trends in ferromagnetic alloys that led them to postulate a spin-orbit interaction as the mechanism

for AMR. Any discussion of this effect should begin with a simple derivation of the spin-orbit energy.

Consider figure 2.1(a) where an electron is traveling in some closed orbit (for example, an energy level) around a nucleus. This figure depicts a simple atom from the rest-frame of the nucleus. This atom will have a total magnetic moment **J** that will depend upon the spin contribution, $\mathbf{S}=\Sigma\mathbf{s}_i$, from the electron and its orbital contribution, $\mathbf{L}=\Sigma\mathbf{l}_i$, from the path the electron follows around the nucleus. The details of **J** will be given by Hund's rules where $\mathbf{J} = |\mathbf{L}-\mathbf{S}|$ for a less than half filled energy level and $\mathbf{J} = \mathbf{L}+\mathbf{S}$ for a more than half-filled energy level. So far nothing new has been added to this quantum mechanical picture.

Now consider figure 2.1(b). In this figure the atom is viewed from the rest frame of the electron. In other words, this figure considers the motion of the nucleus relative to the electron (Einstein enters the picture!). From the viewpoint of the electron, it appears as though the nucleus of charge $+Ze$ travels around it. Using the right hand rule quickly reveals that this circulating charge (an electrical current) produces a magnetic field, **B**. This magnetic field will interact with the intrinsic magnetic moment of the electron (its spin **s**). While figure 2.1 directly visualizes what is happening with the electron, one can also derive the spin-orbit interaction directly. Dirac's relativistic modification of Schrödinger's equation leads directly to an expression for the spin-orbit energy contribution to the total Hamiltonian operator on the system.

This analysis is fairly straightforward and can be found in most texts on quantum mechanics[14]. It starts by deriving an expression for the **B**-field created by the circulating nuclear charge $+Ze$. The law of Biot-Savart reveals that:

$$\vec{\mathbf{B}} = \left(\frac{\mu_0}{4\pi}\right) \cdot \frac{\vec{\mathbf{j}} \times \vec{\mathbf{r}}}{r^3} = \left(\frac{Ze \cdot \mu_0}{4\pi}\right) \cdot \frac{\vec{\mathbf{v}} \times \vec{\mathbf{r}}}{r^3} \qquad \text{Eq. 2.1}$$

An equivalent expression for the magnetic field can be derived using Maxwell's equations to connect the magnetic field to the electric field of the nucleus:

$$\vec{\mathbf{E}} = \frac{1}{e} \cdot \frac{\partial V}{\partial r} \cdot \frac{\vec{\mathbf{r}}}{r} \qquad \text{Eq. 2.2}$$

$$\vec{\mathbf{B}} = \frac{-1}{c^2} \cdot \vec{\mathbf{v}} \times \vec{\mathbf{E}} \qquad \text{Eq. 2.3}$$

In the above equations, V is the atomic potential, e is the charge on the electron, c is the speed of light, μ_0 is the permeability of free space, and Z is the atomic number of the atom. Inserting the equation 2.2 into the equation 2.3 gives:

$$\vec{\mathbf{B}} = \frac{-1}{e \cdot c^2 \cdot r} \cdot \frac{\partial V}{\partial r} \cdot \left(\vec{\mathbf{v}} \times \vec{\mathbf{r}}\right) \qquad \text{Eq. 2.4}$$

Now use can be made of the definition of angular momentum, namely **L**=**r** x **p** and **p**=m**v**. Reversing the cross product eliminates the minus sign and now the expression for the **B**-field of the nucleus involves the orbital angular momentum:

$$\vec{\mathbf{B}} = \frac{1}{emc^2 \cdot r} \cdot \frac{\partial V}{\partial r} \cdot \vec{\mathbf{L}} \qquad \text{Eq. 2.5}$$

The potential energy of a magnetic moment in an applied field is given by the dot product of the moment with the field. The magnetic moment of the electron is $\mu_S = -g\mu_B m_s = -g\mu_B \frac{S}{h}$. Thus:

$$U = -\mu_s \cdot \vec{\mathbf{B}} = \frac{g\mu_B}{emc^2 h} \cdot \frac{1}{r} \frac{\partial V}{\partial r} \cdot \vec{\mathbf{L}} \bullet \vec{\mathbf{S}} \qquad \text{Eq. 2.6}$$

The above derivation was done in the rest-frame of the electron. It is important to go back to the nuclear rest-frame. By doing this, we can express the spin on the electron as $g\mu_B = \frac{eh}{m}$ and we must introduce the Thomas correction factor of 1/2. Therefore, the change in energy due to the spin-orbit coupling is given by:

$$\Delta E_{so} = \frac{1}{2m^2 c^2 \cdot r} \frac{\partial V}{\partial r} \cdot \vec{\mathbf{L}} \bullet \vec{\mathbf{S}}$$

If we assume a Coulomb-type potential for V and consider a p-electron, then the energy change is on the order of 10^{-4} eV/atom and the **B**-field produced by the nucleus is approximately 1 Tesla. This derivation shows us that the **B**-field of the nucleus has sufficient strength to affect the relative orientation of the electron's spin. In fact, Hund's third rule comes from a minimization of this spin-orbit energy. This spin-orbit energy usually appears in the context of the energy spectrum of an atomic electron state, for

instance, the atomic fine structure. However, a conduction electron can have its energy perturbed by this spin-orbit energy when the electron scatters from a magnetic impurity. This feature will be useful in explaining AMR in ferromagnetic materials.

2.1.2: AMR in 3-d Ferromagnets

While 3-d transition metals and their alloys are the most widely used in sensor applications, they remain the least understood of all magnetic materials. What makes these elements unique is the fact that the electrons responsible for their magnetic properties are the same electrons that contribute to bonding in these materials. Simply estimating the total magnetic moment for a ferromagnetic element and comparing it to the measured value most easily demonstrates this. For example, using Hund's rules on iron, Fe ($3d^6 4s^2$), gives the following results: S=2, L=2 and J=L+S=4. Thus, 4 Bohr magnetons are expected per atomic Fe^{2+} atom in the compound Fe_2O_3. However, if one measures a sample of pure metallic iron in a magnetometer it is found to have a saturation moment of only 2.2 Bohr magnetons per iron atom. Because the 3-d electrons contribute to the bonding between iron atoms along with the 4s electrons, the orbital angular moment (**L**) is essentially 'quenched' and does not contribute much to the total saturation moment of the material. The same is true for nickel, cobalt and many transition metal alloys. While this may seem a disadvantage at first, it actually leads to some fairly complicated and interesting properties.

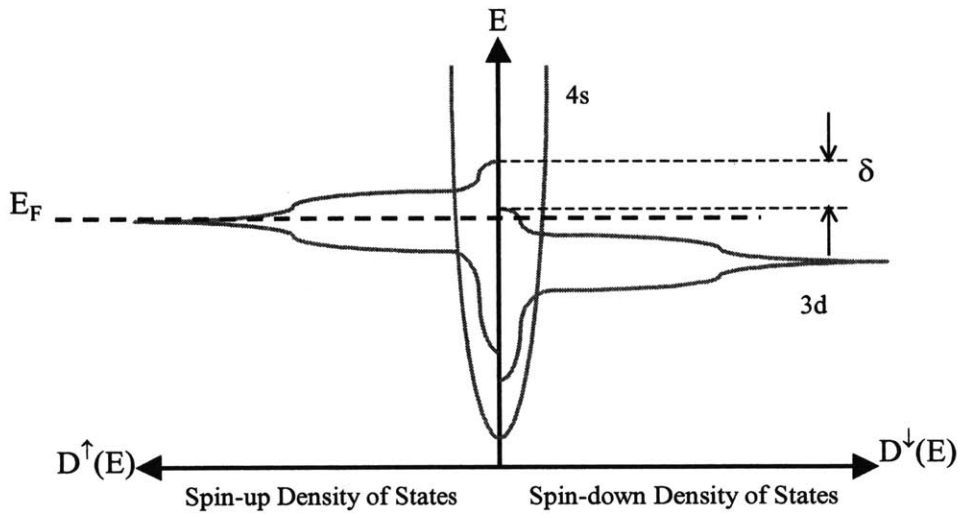

Figure 2.2: The band model of ferromagnetism. In this model the 3d band is split by an energy δ that causes a net polarization of carriers. Notice that 3d electrons dominate the density of states near the Fermi level.

In 1938, E.C. Stoner put forth a model of metallic ferromagnetism where the electron population is split in a spin-up band ($n^{\uparrow}$) and a spin-down band ($n^{\downarrow}$)[15]. The bands are then rigidly shifted in energy by an amount δ, which creates a net polarization of carriers ($n^{\uparrow} \neq n^{\downarrow}$). Figure 2.2 illustrates the band model of ferromagnetism using simple figures for both the s- and d-bands. While variations of this model for ferromagnetism have been considered[16], the Stoner model is by far the most widely accepted.

So why should long range ferromagnetism exist at all in these materials? This question is also somewhat debated in the literature, but the most widely accepted model is the itinerant d-electron model[17]. This model asserts that a small fraction of the localized d-electrons mix with the s-electrons (*s-d* hybridization) and carry with them the magnetic information of the atom. Therefore, ferromagnetic alignment of nearest neighbor

Table 2.1: A comparison of room temperature resistivities and maximum magnetoresistive ratios. ***(Adapted from reference [21])***

Material	ρ (μΩ–cm)	$(\Delta\rho/\rho)_{max}$ (%)
Ni	10.7	2.0
Fe	15	0.8
Co	10.3 (c-axis), 5.5 (basal plane)	~2.0
$Ni_{0.8}Fe_{0.2}$	~20	4.2
$Ni_{0.9}Fe_{0.1}$	~20	5.2

moments occurs through electron mediation. Band structures calculated for Fe and Ni clearly show mixed *s-d* states while photoemission experiments demonstrate the existence of the energy shift, δ. AMR can now be explained in 3-d transition metals.

Consider an electron current moving through the crystal lattice of a 3-d ferromagnet. According to the above argument, there is a high probability that some of these electrons will be scattered into the flatter, lower mobility d-bands that have a higher density of states near the Fermi energy. Because of this s-d scattering, electrons now occupy a d-band and acquire a non-zero angular momentum ($\mathbf{L} \neq 0$). The electrons can have either a positive or negative angular momentum.

Now consider the application of an external magnetic field that induces a magnetization **M** in the sample. This field separates the conduction electrons into two populations, majority (spin-up) electrons and minority (spin down) electrons. Spin-up

electrons have their magnetic moments aligned parallel with the magnetization while spin-down electrons are aligned anti-parallel to the magnetization. The electrical current is now being carried in parallel by two conduction pathways, $\rho^{\uparrow}$ and $\rho^{\downarrow}$. This is referred to as the two-current conduction model, which was first proposed by Mott[18] in 1936.

Taking into account the above information, an electron traveling through the lattice will experience a Coulomb potential (V_C), a spin-orbit potential (V_{so}) and any other scattering potentials (impurities, defects, etc.). The only potential that will depend on the orientation of the magnetic field will be the spin-orbit potential. The angular momentum will be determined by the current direction (**L**=**r** x **p**, **p**=m**v**, and **j**=-ne**v**) and the spin direction will be determined by the magnetization. During a scattering event both majority and minority electrons acquire an angular momentum that could be either positive or negative. If the density of d-states, $D^{\sigma}(E_F)$, near the Fermi level were equal for both the spin-up and spin-down channels, then no AMR effect would be seen since there would be equal probability of scattering into a spin-up or spin-down d-states. Essentially, the separate spin-orbit effects on each channel would statistically cancel out. However, the energy shift (δ) causes an unequal density of d-states at E_F thereby altering the magnitude of V_{so} in each channel. This unequal potential between channels causes one band to become more conductive then the other band. This is seen as a change in resistance of the material as the magnetization is rotated with respect to the current direction.

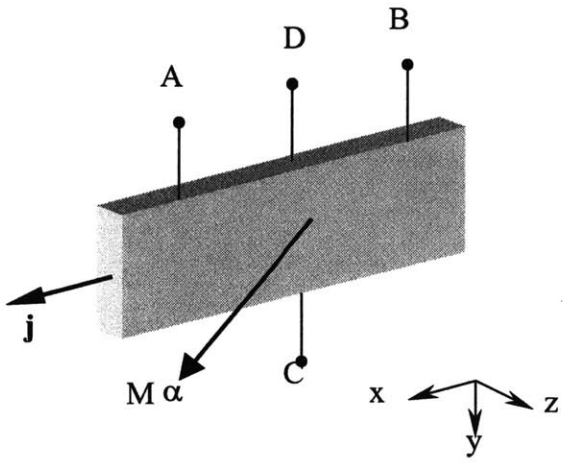

Figure 2.3: A ferromagnetic sample with electrical contacts A, B, C, and D. j is the current density vector, *M* is the magnetization, and α is a unit vector that establishes a direction for M. *(Adapted from reference [18]).*

For most ferromagnetic materials, this effect produces no more than a 6% change in resistivity at room temperature. Table 2.1 shows a list of some common magnetic materials along with their $\Delta\rho/\rho$ and ρ values.

2.2: Phenomenological Aspects of AMR

2.2.1: Resistivity in Ferromagnetic Materials

Figure 2.3 shows an experimental sample of a 3-d transition metal ferromagnet with the necessary geometry for making transport property measurements. Like most material properties, the resistivity can be expressed in the form of a tensor, ρ_{ij}. Although not explicitly proven here[19,20], the tensor has the form:

$$\rho_{ij} = \begin{pmatrix} \rho_{\perp} & -\rho_H & 0 \\ \rho_H & \rho_{\parallel} & 0 \\ 0 & 0 & \rho_{\parallel} \end{pmatrix} \qquad \text{Eq. 2.7}$$

The electric field **E** in the material may now be expressed in the following form:

$$\vec{\mathbf{E}} = \rho_{\perp}(H)\cdot\vec{\mathbf{j}} + \left[\rho_{\parallel}(H) - \rho_{\perp}(H)\right]\cdot\left[\vec{\alpha}\bullet\vec{\mathbf{j}}\right]\cdot\vec{\alpha} + \rho_{H}(H)\left(\vec{\alpha}\times\vec{\mathbf{j}}\right) \qquad \text{Eq. 2.8}$$

In equation 2.8, **j** is the current density vector, α is a unit vector that points in the direction of the magnetization (**M** = M(H) α). $\rho_{\parallel}(H)$ is the resistivity of the sample when **M** is parallel to **j**, and likewise, $\rho_{\perp}(H)$ is the resistivity when **M** is perpendicular to **j**. $\rho_{H}(H)$ is the extraordinary Hall resistivity and will not be used in any further analysis. Ohm's law allows us to connect the electric field to the current density, which can be written in a very compact form:

$$\rho = \frac{\vec{\mathbf{E}}\bullet\vec{\mathbf{j}}}{\left|\vec{\mathbf{j}}\right|^{2}} \qquad \text{Eq. 2.9}$$

We can now use figure 2.3 and equations 2.8 and 2.9 to derive an expression for the resistivity as a function of angle between the magnetization, **M**, and the current density, **j**. This derivation assumes that the current density is in the x-direction only and that **M** is free to rotate in the x-y plane. Substituting equation 2.8 into equation 2.9 gives:

$$\rho(H) = \rho_{\perp}(H)\cdot\frac{\vec{\mathbf{j}}\bullet\vec{\mathbf{j}}}{\left|\vec{\mathbf{j}}\right|^{2}} + \left[\rho_{\parallel}(H) - \rho_{\perp}(H)\right]\cdot\frac{\left\{\left[\vec{\alpha}\bullet\vec{\mathbf{j}}\right]\cdot\vec{\alpha}\right\}\bullet\vec{\mathbf{j}}}{\left|\vec{\mathbf{j}}\right|^{2}} + \rho_{H}(H)\frac{\left(\vec{\alpha}\times\vec{\mathbf{j}}\right)\bullet\vec{\mathbf{j}}}{\left|\vec{\mathbf{j}}\right|^{2}} \qquad \text{Eq. 2.10}$$

The third term of this equation is automatically zero from the assumptions stated above. This equation reduces to the following form:

$$\rho(H) = \rho_{\perp} + [\rho_{\parallel} - \rho_{\perp}] \cdot \frac{|\vec{\alpha}|^2 \cdot |\vec{j}|^2}{|\vec{j}|^2} \cdot \cos^2(\theta) = \rho_{\perp} + [\rho_{\parallel} - \rho_{\perp}] \cdot \cos^2(\theta) \qquad \text{Eq. 2.11}$$

The field dependence of the resistivities has been omitted to simplify the look of equation 2.11. θ is the angle between the magnetization and the current vector. Since a ferromagnetic material's resistivity depends upon its state of magnetization, an average resistivity and a resistivity anisotropy are defined, respectively, as:

$$\rho_{ave} = \frac{1}{3} \cdot \mathrm{Tr}(\rho_{ij}) = \frac{\rho_{\parallel} + 2\rho_{\perp}}{3} \qquad \text{Eq. 2.12}$$

$$\frac{\Delta\rho}{\rho} = \frac{\rho(H) - \rho_{ave}}{\rho_{ave}} = \left(\frac{\Delta\rho}{\rho_{ave}}\right)_{\max} \left(\cos^2\theta - \frac{1}{3}\right) \qquad \text{Eq. 2.13}$$

In this geometry $\rho_{\perp} < \rho_{\parallel}$. This affect, called anisotropic magnetoresistance, will now form the basis of a sensor design. Before discussing sensor design, θ must be related to the set of magnetic properties, including the anisotropy field, H_a, and external magnetic field, H.

2.2.2: Magnetization Processes

At this point, it is important to connect the concept of a magnetic hysteresis loop with some of the features of a magnetoresistance plot, that is, $\Delta\rho/\rho$ versus an applied external field. The following discussion focuses mainly on the soft, ferromagnetic materials used as active elements for magnetic field sensors. It is the intention of this section to link the angle θ to the applied magnetic field, H.

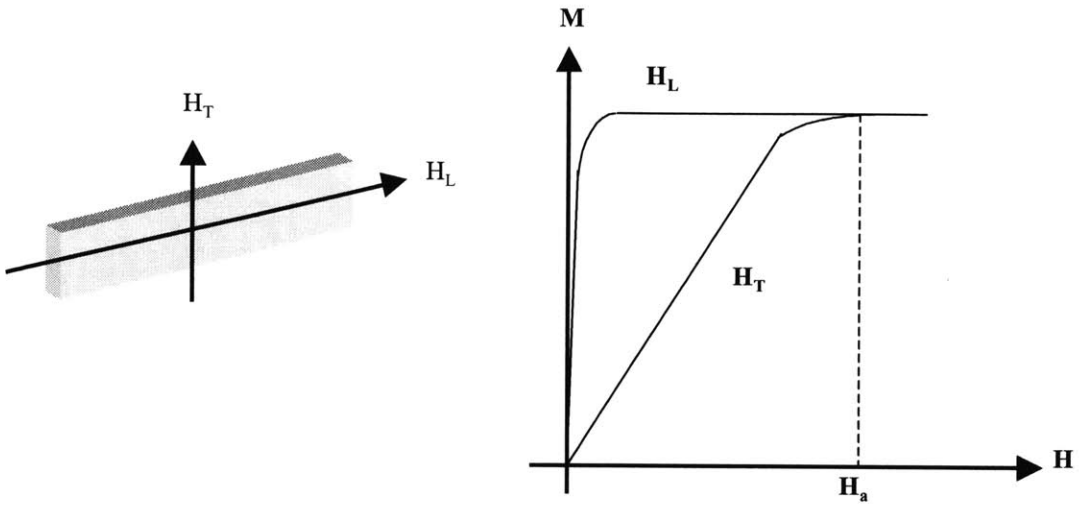

Figure 2.4: A plot of a soft ferromagnetic material. H_T is the transverse field and H_L is the longitudinal field. H_a is the anisotropy field.

Figure 2.4 shows a plot of the magnetization of a rectangular, ferromagnetic sample versus the applied field. The field is applied along the length or width of the sample.

The most obvious difference in the two plots of figure 2.4 is that the M-H loop for the transverse field is sheared over with respect to that for the longitudinal field. This shearing effect is due to *shape anisotropy*, in other words, it is harder to magnetize the sample along its width than along its length. This type of anisotropy comes from the formation of magnetically charged surfaces that produce an internal demagnetizing field, H_D. Demagnetizing fields can be easily calculated for various shapes using tabular data of demagnetizing factors[21]. As two magnetically charged surfaces come closer together, the demagnetization field increases, making it harder to reach saturation. Shape effects

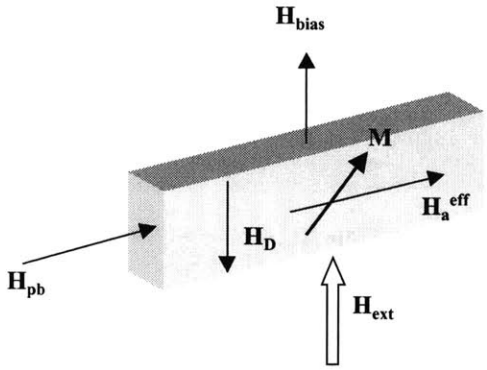

Field	Approx. Strength	Description
H_{bias}	~200 Oe	SAL bias field to orient M at 45 degree angle
H_{ext}	Variable	External field to be measured
H_D	~100 Oe	Demagnetization field
H_a^{eff}	~5-20 Oe	Effective anisotropy field
H_{pb}	8-10 Oe	Parallel bias field to reduce domain formation and noise

Figure 2.5: An idealized rectangular sensor element showing the various fields. The table briefly describes the fields and their associated magnitudes.

can be a significant source of magnetic anisotropy in thin film sensors and are used in the design of magnetic sensors.

Other forms of magnetic anisotropy include magnetocrystalline anisotropy, field-induced anisotropy, and magnetoelastic anisotropy. Magnetocrystalline anisotropy results from the coupling of the magnetization with specific directions in the crystal lattice. This anisotropy can be large or small depending on the types of materials used. Field induced anisotropy occurs from application of an external magnetic field during thin film growth or annealing. A field induced easy axis can be imposed on an otherwise isotropic sample, such as a circular disk that has no in-plane shape anisotropy. Finally, magnetoelastic anisotropy comes from the coupling of film strain (or stress) to the magnetization. This type of anisotropy can be controlled by careful consideration of thin film stresses and by choosing material compositions that show low magnetostriction.

Figure 2.5 shows a picture of a sensor element with all of the pertinent fields that can affect the direction of magnetization in the material. This figure can be used to analyze the rotation of the magnetization in the sensor. Before this analysis begins, it is necessary to describe the different fields involved. **M** is the magnetization vector of the sensor material. In order to obtain the largest change in resistance, the magnitude of **M** should be close to its saturation value: $|\mathbf{M}| = M_s$. H_D is the demagnetizing field produced by the magnetization of the sensor. H_{ext} is the external magnetic field that the sensor detects (such as the fringe field from disk storage media). H_{bias} is a bias field that is used to cant the magnetization **M** at 45 degrees with respect to the current direction. This bias field can be designed into the sensor element. The origins of this bias field will be discussed in section 2.3 of this chapter. H_a^{eff} is the effective anisotropy field that causes the magnetization to rotate parallel to the current direction. The origins of this field can come from the shape of the element or can be induced by field annealing. Finally, H_{pb} is a parallel bias field used to eliminate domain formation in the sensor. Domains present in a sensor will not only cause a random distribution of magnetization, but also move in an unpredictable manner when exposed to an external field. This causes noise in a sensor element.

An analysis of the magnetization rotation starts under the assumption that the external field, as well as the other fields, are uniform across the whole sensor and that the sensor itself contains no domains. Therefore, the rotation of the magnetization vector away from the easy axis direction is governed by the magnetostatic and anisotropy

energies of the system. A good derivation of the relevant fields affecting **M** can be found in reference [21]. Only a summary of these fields will be given here:

1) The anisotropy energy, K_u, produces a component of the effective anisotropy field. It's free energy can be expressed as $K_u \sin^2 \theta$. θ is the angle the magnetization makes with respect to its easy axis.
2) The vertical bias field from the SAL, $-M_s H_{bias} \sin \theta$
3) The parallel bias field used for noise reduction, $-M_s H_{pb} \cos \theta$
4) The external field, $-M_s H_{ext} \sin \theta$

By adding all of these free energies together and taking the derivative to find the zero torque condition, an *M-H* plot can be generated. **M** in figure 2.5 will rotate under the following condition:

$$\frac{M_y}{M_s} = \sin\theta = \frac{H_{bias} + H_{ext}}{H_a^{eff} + H_{pb}} \qquad \text{Eq. 2.14}$$

$$\cos^2\theta = 1 - \sin^2\theta \qquad \text{Eq. 2.15}$$

Substituting equations 2.14 and 2.15 into equation 2.13 (see page 29) will yield:

$$\frac{\Delta\rho}{\rho} = \left(\frac{\Delta\rho}{\rho_{ave}}\right)_{\max}\left[\frac{2}{3} - \left(\frac{H_{bias} + H_{ext}}{H_a^{eff} + H_{pb}}\right)^2\right] \qquad \text{Eq. 2.16}$$

The above equation now links the fields affecting the sensor to its change in resistance.

2.3: Sensor Design

The subject of AMR sensor design is vast and has had ample representation in the literature. The first description of a sensor based on the AMR effect was given by Hunt[22]

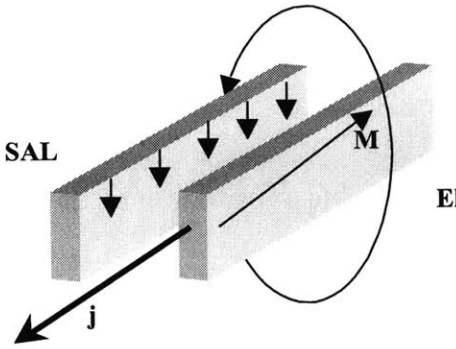

Element	Thickness	Properties
MR Layer	<200 Å	Low resistivity
Spacer	~30-50 Å	High ρ, >100μΩ-cm
SAL	<200 Å	$\rho_{SAL} > \rho_{MRE}$

Figure 2.6: A SAL biased MR element. The SAL provides a bias field when fully saturated by primary field of the MR element. This bias field from the SAL couples to the MR element by a dipole interation.

in 1971. Later, Thompson *et al.*[23] wrote a review of the various sensor designs that could be used for storage and memory applications. Since a detailed description of sensor design is outside the scope of this thesis, a brief description of only one such design, the soft-adjacent layer (SAL) bias design, will be given. The rest of the section will focus on the processing techniques used in the fabrication of a sensor and how these techniques can affect sensor performance.

2.3.1: SAL Biased Sensors

Figure 2.6 shows a SAL biased AMR element. As stated earlier, the soft-adjacent layer is used to create a bias field that will cause the magnetization, **M**, to rotate to 45 degrees with respect to the current, **j**. This bias field is produced in a simple way. The current is allowed to flow through the entire structure of Figure 2.6. The current that flows through the MR element produces a primary magnetic field (using the right-hand rule) that saturates the SAL in the vertical direction. The saturated SAL then produces a

bias field that couples to the MR element's magnetization by a dipole interaction. The thickness' of the MR element and SAL as well as the SAL's saturation moment are adjusted to follow the equation $M_s \cdot t_{SAL} = M_r \cdot t_{MRE}$, where t_{SAL} and t_{MRE} are the thickness of the SAL and MR elements, respectively.

Also, to get the maximum MR response, the resistivity of the SAL and spacer are designed so that most of the current flows through the MR element. The table in figure 2.6 describes some of the features of an AMR sensor.

2.3.2: Fabrication Techniques

By far the most commonly used thin film deposition technique is magnetron sputtering[14]. Sputtering is a physical vapor deposition (PVD) process by which an ionized noble gas, such as argon, is accelerated towards a target composed of the material to be deposited. The impact of the ionized atoms liberates material from the target surface. This 'sputtered' material then travels towards and deposits on the substrate thus creating the desired film. Background gas pressure is usually in the range of 5-20 mTorr in order to sustain a cathode voltage of approximately -200V to -500V. Multilayered films are easily fabricated using several magnetron sources and a shutter system. Typical substrates used for deposition are amorphous oxides like silica glass or alumina. Target materials can be made of pure metals or alloys (DC or RF magnetron sputtering) and insulators (RF magnetron sputtering only).

PVD sputtering can allow for precise control over film thickness down to ±1Å. However, since this is a gas discharge process, the rough vacuum conditions used during deposition allow for diffuse scattering of the depositing species. This can cause non-uniformities in film thickness over the sample surface as well as uncontrolled film stresses due to incorporated gases. The gas used to create the plasma must come from ultra-pure sources. Therefore the gas lines into the vacuum system need to be contamination free. Vacuum systems with load-locks can reduce the need for opening a system to atmosphere, but low background pressures should be maintained to reduce the risk of film contamination.

Since magnetic thin films are sensitive to both composition and structure, PVD sputtering must be used carefully. Changes in film composition can affect the saturation moment of a material as well as its anisotropy and resistivity. Chemical mixing at interfaces can 'blur' the structure and cause variations in device properties. As well, porous structures can lead to high coercivity and large resistivities while also allowing for significant diffusion of other surrounding materials. These are just some of the issues associated with deposition of thin films. All these issues must be addressed in order to have a device that operates according to its design.

CHAPTER 3: EXPERIMENTAL

Chapter 3 deals with the fabrication techniques involved in producing multi-layered magnetic thin-films as well as the characterization tools used. Section 3.1 describes the vacuum deposition system built for making the magnetoresistive samples. This section focuses on the test samples and the details of the vacuum deposition conditions. A standard protocol is given for cleaning the substrate, de-gassing the substrate, and deposition of each sample.

Section 3.2 focuses on the characterization techniques used to determine the properties of each sample. In this section, the basics of vibrating sample magnetometry (VSM) and four-point probe resistivity measurements will be described. A design of an *in-situ* four-point MR probe is given as well.

3.1: Sample Preparation

3.1.1: Experimental Samples

In order to test new materials for use in AMR sensors, it is important to create a multilayer film that consists of a non-magnetic seed layer, a ferromagnetic AMR layer, and a non-magnetic capping layer. The seed layer is analogous to the spacer layer of an AMR sensor and the capping layer of the sample will serve as the protective coating against oxidation. In both cases, the substrate is a non-conductive oxide. Amorphous silica glass is a good choice for a substrate since it is cheap, abundant, and has very little surface roughness. Table 3.1 shows a list of the materials used in commercial AMR sensors along with a list of their desired properties. The values in parentheses represent the materials used in this study. The overall structure of the test samples is given in the last row of the table.

Table 3.1: This table shows some of the desired properties for a magnetoresistive element. The values in parentheses are the values or materials used in this thesis. The last row describes the multilayer films prepared for this study.

	Seed and Capping Layer		**MR Layer**
	Present	**Proposed**	
Material	β-Ta	$Ni_{80}Cr_{20}$	$Ni_{81}Fe_{19}$
Resistivity (μΩ-cm)	200	120	20-30
Thickness (Å)	100	50	200
Magnetic Order	non-magnetic	non-magnetic	Ferromagnetic
Lattice Constant (Å)	a=10.2, c=5.3	a=3.54	a=3.54
Test Samples	**a-SiO_2(0.16mm) / NiCr(50Å) / NiFe(200Å) / NiCr(50Å)**		

3.1.2. Sample Preparation Protocol

Samples prepared for this study followed a standard protocol for cleaning, de-gassing, and deposition. The protocol is as follows:

1. Ultrasonically wash ϕ22 mm x 0.16 mm glass slide (VWR #48380-068) in acetone for 5 minutes, then in ethanol for 5 minutes and finally in methanol for 5 minutes. Blow dry using compressed gas (Chemtronics UltraJet duster).

2. Mount substrate onto stainless steel sample holder (MDC P/N STA-1) using Kapton™ tape adhesive (1-mm x 6-mm lengths).

3. Load substrate holder onto transfer arm (MDC P/N STA-2) in load-lock and close entry door. Rough pump load-lock to less than 1mTorr of pressure.

4. Introduce substrate holder into main chamber and load sample holder onto sample dock (MDC P/N STA-3). Remove the sample transfer arm, close gate valve and allow main chamber pressure to return to UHV level ($< 5 \times 10^{-8}$ Torr).

5. De-gas substrate using the 150°C set point on the temperature controller for 1 hour. Wait for sample temperature to stabilize or wait for main chamber pressure to drop below 1×10^{-8} Torr. **(Note: actual sample temperature ~100°C as measured by an in-situ J-Type thermocouple and read from external Omega HH-26J digital thermometer)**

6. Ramp temperature controller from 150°C to 350°C set point (actual sample temperature ~200°C) and allow the sample temperature to stabilize.

7. Lower gate valve between the turbo pump (Sieko-Sieki Model STP-400) and main chamber but do not fully close. Back fill chamber with high purity argon (99.995% pure Ar) and stabilize pressure to 10 mTorr. Allow 5 minutes for temperature and pressure to stabilize.

8. Turn on substrate bias power supply and set to -200V.

9. Turn on cooling water for DC magnetron sputter sources. Set DC power-supplies to 50W and allow magnetron sources to sputter for 5 minutes with shutters closed. Lower power to 20W and open shutter of NiCr source. Sputter 50Å of material (approximately 44 sec).

10. Close the shutter, return the power supplies to 0W and shut off high voltage switch, close the gas source and cooling water. Wait 30 seconds for main chamber pressure to drop below 0.1 mTorr and then re-open turbo pump gate valve.

11. Anneal sample at T=200°C for a specified period of time (0.5, 3, 10, and 24 hours).

12. Return the temperature controller set point to 150°C and allow for sample temperature to stabilize. Deposit remaining films (200Å NiFe and cap with 50Å NiCr) at T=100°C.

13. Transfer the sample from the main chamber to the load lock and remove sample for testing.

All samples were prepared following this protocol. Five samples were prepared to investigate the impact of a new seed layer, $Ni_{80}Cr_{20}$, on the magnetoresistive properties of the Permalloy, $Ni_{81}Fe_{19}$, layer. The annealing experiments were used to study the possible role of seed layer microstructure on MR properties. Table 3.2 shows a list of the samples made:

Table 3.2: A table of the samples prepared in this study.

Sample	Anneal Time (ks)	Anneal Temperature (°C)	Sample Bias
AMMR200	As-deposited	None	-200V and 86 Oe
AAMMR5	1.8	200	-200V and 86 Oe
AAMMR03	10.8	200	-200V and 86 Oe
AAMMR10	36.0	200	-200V and 86 Oe
AAMMR24	86.4	200	-200V and 86 Oe

The samples described in Table 3.2 were deposited using a negative bias voltage and a magnetic field bias on the sample during deposition. Negative bias voltages have been used in many situations to affect film properties[25]. Biased sputtering can increase film density while decreasing porosity. Also, films deposited under an electrical bias can show a bulk-like resistivity. Depositing in a magnetic bias field imparts an easy axis on the sample. Magnetic films deposited on circular glass substrates have no in-plane easy direction (no shape anisotropy). So, a magnetic bias field of 86 Oe is used to impart magnetic anisotropy in the sample. This induced anisotropy is important and can be used to design sensors with a specific easy direction. In the case of the samples in Table 3.2, the easy direction is along the same axis as the bias field.

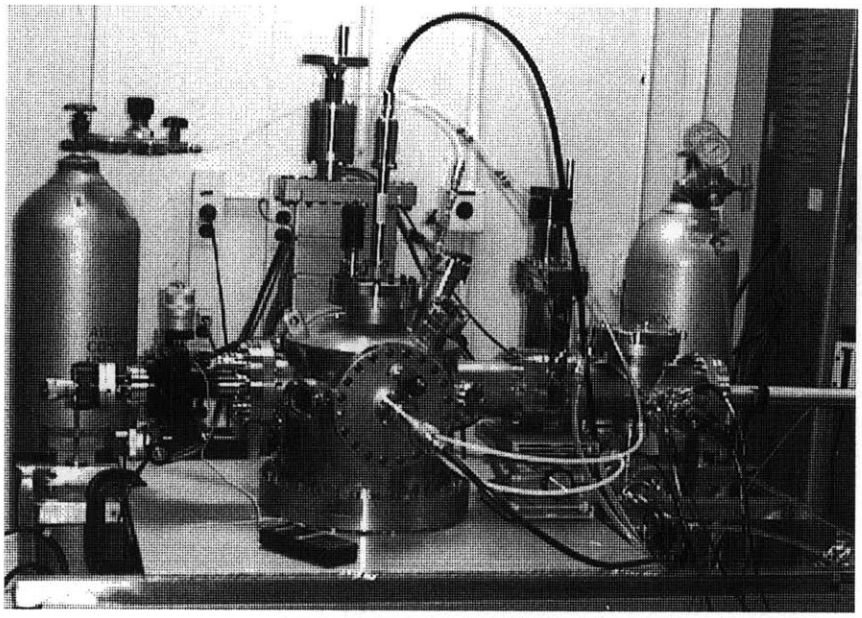

Figure 3.1: A digital picture of the vacuum system used to deposit samples.

3.1.3: Sample Deposition System

Figure 3.1 shows a digital picture of the vacuum deposition system used to fabricate the samples studied in this thesis. This vacuum system was built for the purpose of DC magnetron sputtering. It has the following features:

1. A Seiko-Seiki 400 L/s Turbo Pump (Model STP400). Ultimate base pressure is 8 x 10^{-9} Torr.

2. Two magnetron sputter sources (Kurt J. Lesker Co.) for up to a 1kW DC or 500W RF power.

3. High precision translation sample manipulator (Vacuum Generators Model #HPT-102) with a Watlow *in-situ* coil heater and CyberTherm power controller. Capable of temperatures from 25°C to 300°C. DC electrical sample bias and magnetic field biases are also available.

4. Optional Perkin-Elmer Physical Electronic ion-gun.

5. Manual gas control system (0.15 to 50 mTorr)

As mentioned above, the deposition method used is DC magnetron sputtering. A good description of sputtering as well as other deposition methods can be found in reference [24].

3.1.4: Vacuum Deposition Conditions

The sample preparation described in section 3.1.2 gave the steps for making a multilayer sample. Since deposition conditions, such as substrate temperature, substrate bias, background pressure, etc., can significantly alter film properties, it is important to maintain the same conditions from sample to sample. For example, the maximum power available to the magnetron source is proportional to the pressure of the sputtering gas (argon in this case) in the chamber. Unless a constant power is maintained by the power supply, fluctuations in chamber pressure can cause fluctuations in the deposition rate. This assumes that a separate deposition rate meter is not being used. As alluded to above, sample bias has a direct impact on many material properties. By applying a negative sample bias, positively charged atoms (argon and other ions) are attracted by the sample surface and re-sputter the depositing species. The 'peening' action of these ions also densifies a film and reduces the number of voids in a sample. Good control over substrate temperature can allow atoms to have significantly more surface mobility. A good discussion of this subject can be found in references [24] and [25]. Table 3.3 lists the conditions under which the samples for this study were made.

Table 3.3: Some depositon conditions for the samples made.

	Seed Layer	MR Layer	Capping Layer
Substrate Temperature	200°C	100°C	100°C
Electrical Bias	-200 V	-200 V	-200 V
Magnetic Field Bias	86 Oe	86 Oe	86 Oe
Deposition Pressure	10 mTorr	10 mTorr	10 mTorr
Base Pressure	1 x 10^{-8} Torr	1 x 10^{-8} Torr	1 x 10^{-8} Torr
Cathode Power	20 W	20 W	20 W
Deposition Rate	1.3 Å/s	1.1 Å/s	1.3 Å/s

3.2: Sample Characterization Techniques

3.2.1: Vibrating Sample Magnetometry (VSM)

The magnetic properties of the samples are measured using Digital Measurement Systems' vibrating sample magnetometer (VSM Model 880A). The VSM is a fast and simple technique that directly measures the magnetic moment of thin films and bulk samples. Figure 3.2 on the next page illustrates the components of a VSM.

A sample is attached to the rigid support arm (usually made of quartz glass) that is connected to the vibrator assembly. The sample is then set equidistant between the pole pieces of an electromagnet. A flat, pancake coil is placed on each end of the poles of the electromagnet and a lock-in amplifier is used to detect the signal. The reference frequency of the lock-in amplifier is also used to determine the drive frequency of the vibrator assembly. Most VSM designs, including the one used in these experiments, use a set of speaker coils to act as the driving mechanism for the vibrator assembly. The pick-up coils are usually a flat, multi-turn set of copper wires each in a figure-eight configuration.

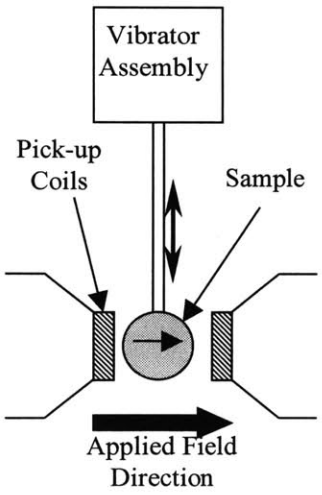

Figure 3.2: A simple schematic of a vibrating sample magnetometer (VSM). The AC voltage signal at the pick-up coils is detected using a lock-in amplifier with a reference frequency set to that of the vibrator assembly.

Measurement of a sample's magnetization is now reduced to measuring the AC voltage signal that develops across the terminals of the pick-up coils. The magnitude of this AC voltage depends directly on the magnetization of the sample. The lock-in amplifier can accurately discern and measure this signal from the background noise of the laboratory. A separate power supply controls the magnetic field produced by the electromagnet. This field is scanned in a stepwise fashion and the user sets the measurement parameters.

Vibrating sample magnetometers measure the total magnetic moment in a sample. The cgs unit of magnetic moment is the electromagnetic unit, or emu. However the emu by itself is meaningless since it depends on the volume of the sample measured (the more magnetic material there is, the more emu's measured). So, in order to make comparisons and use the equations of magnetism, the volume magnetization density, $\boldsymbol{M}$, is used (emu/cm^3). Most commercial magnetometers have a sensitivity of about $5x10^{-6}$ emu. A

emu. A simple check of the Permalloy samples made will determine if this sensitivity is sufficient to make measurements:

$$\mu = \left(\frac{10{,}000}{4\pi} Gauss \right) \cdot V = 795.8 \frac{emu}{cm^3} \times \left(3.801 cm^2 \times 200 x 10^{-8} cm \right) = 6.05 x 10^{-3} emu \qquad \text{Eq. 3.1}$$

This is ~1000 times larger than the lower limit of the magnetometer.

Before using the magnetometer, a calibration of the pick-up coils and applied field is performed. A Hall probe measures the applied field and sends an analogue signal to the control electronics of the VSM. This signal is internally calibrated by the VSM electronics. To calibrate the pick-up coils, a pure nickel disk (99.9995%, ~485emu/cm^3) of known volume is placed in the system and measured at its saturation value. The resulting voltage at the pick-up coils is divided into the calculated moment, giving the system a calibration factor in emu/volt. Once this is completed, the system then measures the diamagnetic signal of the quartz sample holder and subtracts that from the measurement of the sample.

In order to measure the samples made in this study, the calibration procedure was performed using a blank glass substrate attached to the sample holder. This allows the system to subtract out the diamagnetic effects of the substrate. Measuring the bare substrate in the magnetometer shows that the largest signal produced is 10^{-4}emu at 10,000 Oe of applied field. Since the substrate signal is approximately 10% of the Permalloy signal as measured by the pick-up coils, it is important to correct for the diamagnetism of

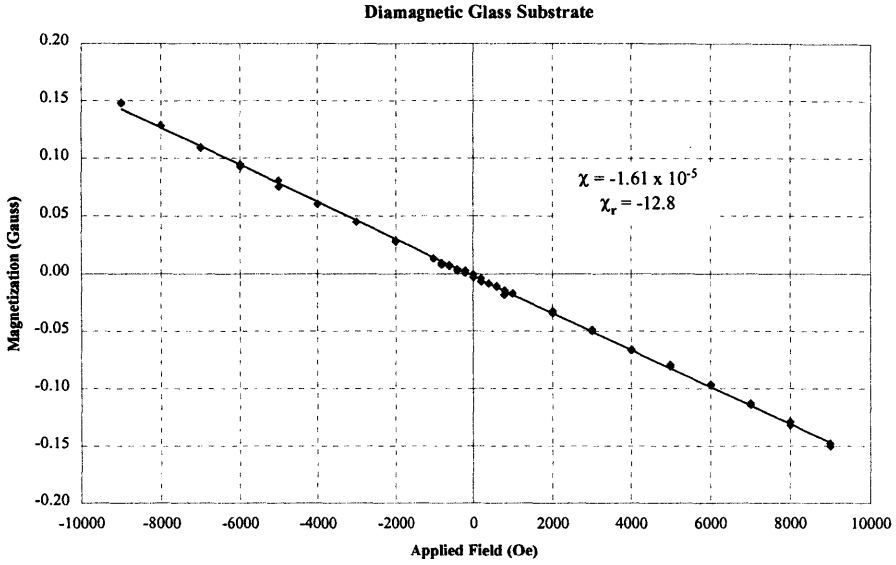

Figure 3.3: A magnetization versus applied field plot for the diamagnetic glass substrates used in this investigation. The relative magnetic susceptibility of this material is approximately -12.8.

the substrate. Figure 3.3 shows an *M-H* plot for a glass substrate. Note that the glass substrate has a relative susceptibility (χ_r) of -12.8.

Samples were assumed to be of uniform thickness and the volume of magnetic material was calculated using the thickness and area of the sample. Magnetic measurements on each sample were made after *in-situ* measurements of their magnetoresistance.

3.2.2: Glancing Incidence X-ray Diffraction (GIXRD)

The Center for Materials Science & Engineering (CMSE) X-ray diffraction facility has a Rigaku 180mm x-ray diffractometer capable of making glancing incidence measurements. GIXRD is a technique whereby the diffractometer is taken out of the Bragg-Brattano mode of operation (θ-2θ mode) and the incident beam is set to a low

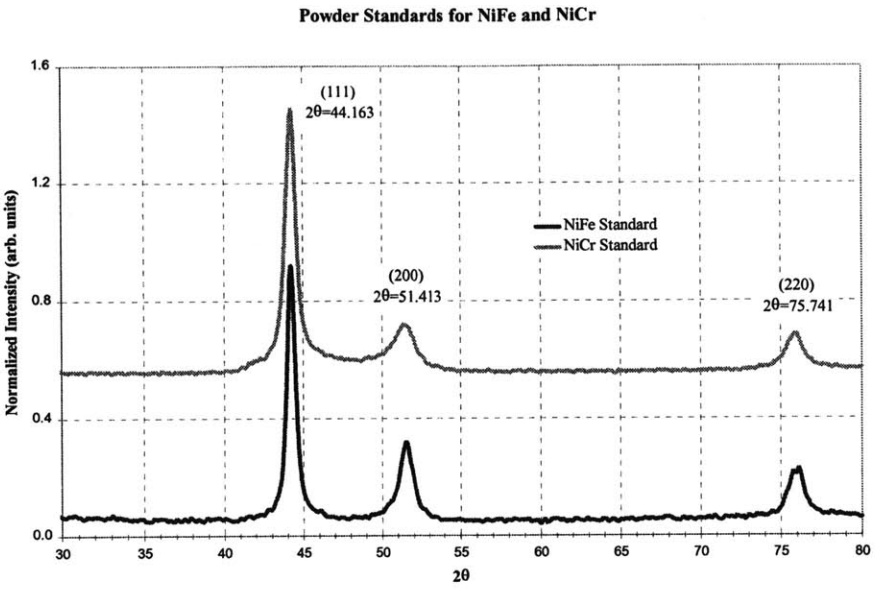

Figure 3.4: A powder diffraction scan of $Ni_{81}Fe_{19}$ and $Ni_{80}Cr_{20}$.

angle ($\theta \approx 1^{\circ}$). The detector is then scanned through the various Bragg angles. Special Soller slits and wider diffraction and receiving slits allow for higher irradiated volumes resulting in a higher output signal at the detector. Further information about X-ray diffraction can be found in reference [26].

All samples were mounted onto a glass sample holder for use in the diffractometer. Two standard powder samples of NiCr and NiFe were prepared to measure the known peak positions for the materials. This data is shown in Figure 3.4. These peak positions allow the determination of in-plane texture for the films. The lattice parameter for each material is approximately 3.5450Å for $Ni_{80}Cr_{20}$ and 3.5489Å for $Ni_{81}Fe_{19}$. More information about the crystal structure of these materials can be found in JCPDS powder diffraction files #04-850 (Synthetic Nickel), #23-297 (Taenite), and #38-419 (Awaruite).

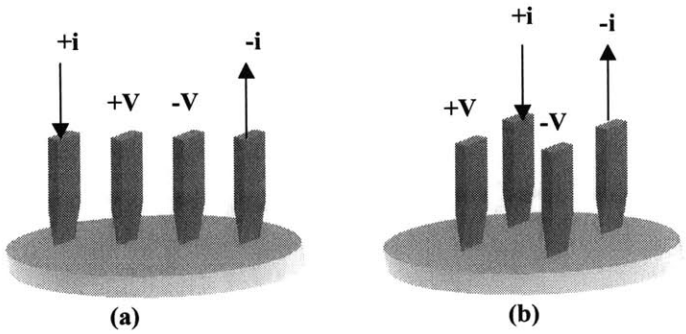

Figure 3.5: Various four-point probe configurations. (a) An evenly spaced linear array. (b) An evenly spaced square array.

3.2.3: Scanning Electron Microscopy (SEM)

Scanning electron microscopy was performed at the CMSE Analytical Spectroscopy Lab. Images of the surfaces of the samples were taken using the Physical Electronics Model 660 Auger Electron Spectroscopy/Scanning Auger Microprobe (AES/SAM) system. Images were taken of the as-deposited, the 3-hour annealed, and 24-hour annealed films. Auger depth profiles were unable to resolve the interfaces in our samples due to the limited sputter depth resolution and the relatively large sampling depth of the Auger electrons (Auger electrons are produced from approximately the first 20Å to 30Å of material).

3.2.4: Magnetoresistance Measurements

Resistivity, ρ, is a fundamental transport property of any material. The four-point probe is the most commonly used measurement method for determining the resistivity of a thin-film material. In this technique, four individual probes contact the material to be measured; two of the probes carry a constant, DC test current and the other two probes measure the potential difference. Four-point probes can be designed to contact the

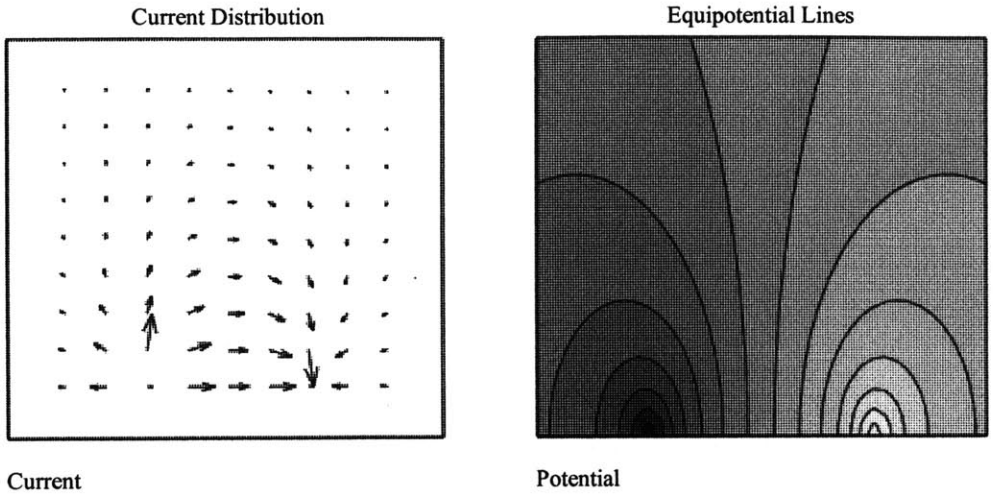

Figure 3.6: Plots of the current distribution and equipotential lines produced by a dipole source. The current flow, I, is perpendicular to the equipotential lines.

sample in a variety of ways, but the most common designs are the linear array and the square array. Figure 3.5 shows the two types of probe arrays. Much theoretical consideration has been given to how these types of probes operate and what differences the geometry makes in the measurement of the resistivity[27,28,29,30,31]. For all four-point probe measurements of magnetoresistance ($\Delta\rho/\rho$), the following expressions are true:

$$\frac{V}{I} = R_s = \frac{\rho}{t_{film}} \cdot f(x,y) \qquad \text{Eq. 3.2}$$

$$\frac{\Delta R_s}{R_s} = \frac{\Delta\rho}{\rho_{ave}} \cdot M_r(x,y) \qquad \text{Eq. 3.3}$$

V is the measured voltage, I is the test current, $f(x,y)$ is a constant factor that corrects for the geometry of the probe and the dimensions of the film measured, and $M_r(x,y)$ is a constant correction factor for the non-uniform flow of current. The origins of $M_r(x,y)$ lie in the fact that the equipotential lines generated by a dipole charge distribution (the two current probes) are non-uniform. Figure 3.6 shows a plot of the equipotential lines and

current flow generated by a dipole charge distribution ($q = \frac{I \cdot \rho}{2\pi}$, I is the current into the plane, and ρ is the resistivity in cgs units). The flow of current is perpendicular to these lines and is, therefore, non-uniform. $M_r(x,y)$ is the correction factor that accounts for this non-uniform flow. The forms of $f(x,y)$ and $M_r(x,y)$ were worked out by Norton in 1983 for a semi-infinite thin film. This paper assumes that the current probes are at the x-y coordinates of (1,0) and (-1,0). It also assumes that the material's resistivity is isotropic with respect to the crystalline axes and that the $(\Delta\rho/\rho_{ave})<<1$. These are good assumptions for Permalloy, which is a cubic material and has less than 4% $\Delta\rho/\rho_{ave}$. The equations for the correction factors are found to be:

$$f(x,y) = \frac{1}{2\pi} \cdot \ln\left[\frac{(x+1)^2 + \left(\frac{\rho_y}{\rho_x}\right) \cdot y^2}{(x-1)^2 + \left(\frac{\rho_y}{\rho_x}\right) \cdot y^2}\right] \qquad \text{Eq. 3.4}$$

$$M_r(x,y) = \frac{y^2}{\ln\left(\frac{r_+}{r_-}\right)} \cdot \left|\frac{1}{r_-^2} - \frac{1}{r_+^2}\right| \qquad \text{Eq. 3.5}$$

$$r_+^2 \equiv (x+1)^2 + y^2$$

$$r_-^2 \equiv (x-1)^2 + y^2$$

If the current probes were located at (±1,0), then a square array would have the voltage probes at (±1,2). Assuming $\rho_x = \rho_y = \rho$, this would give a geometry factor, $f(x,y)$, of $\left(\frac{ln2}{2\pi}\right)$ and a $M_r(x,y)$ factor of $\left(\frac{1}{ln2}\right)$.

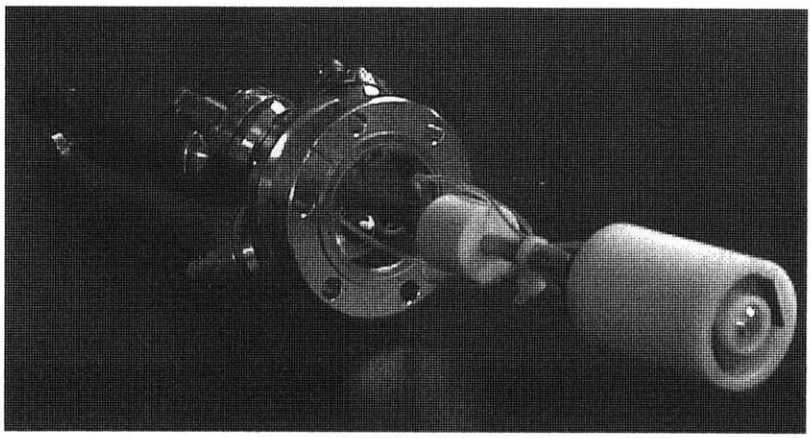

(b)

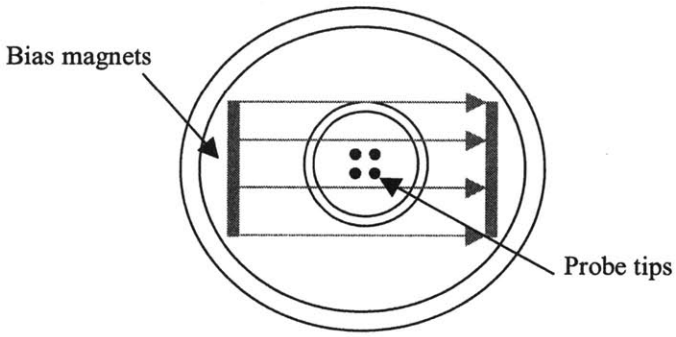

Figure 3.7: (a) A digital image of the *in-situ* magnetoresistance probe. (b) A front view schematic of the MR probe showing the placement of the bias magnets.

In order to measure the magnetoresistance of the films fabricated in this study, an *in-situ* probe was designed. The MR setup used a square four-point probe specially modified for a high vacuum environment. A Keithly Model 196 digital multimeter was used to measure the sheet resistance of the films. An electromagnet assembly set orthogonal to a permanent magnet assembly provided the rotational magnetic field. Figure 3.7 shows a digital image of this setup. A 5A/18V DC power supply provided the current for the electromagnet. The electromagnet was made out of a Permalloy yoke with a 200-turn, 1.6Ω coil capable of producing a 54.9 Oe/A at the midpoint of a 1-inch gap. The permanent magnets are ceramic ferrite rectangles (10mm x 3mm x 1.5mm) and

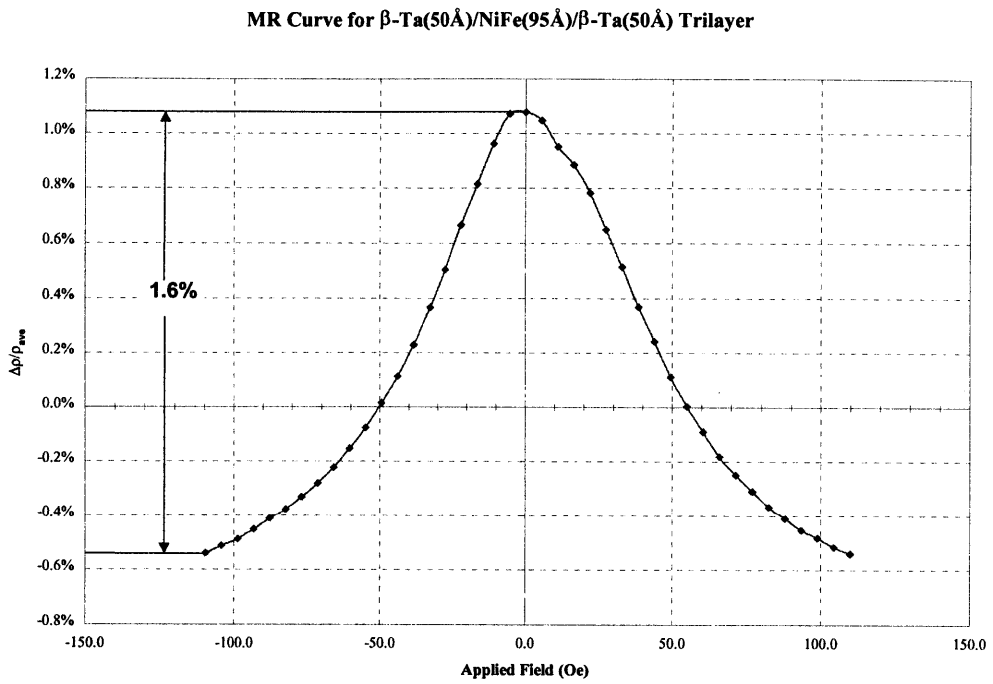

Figure 3.8: A transfer curve for a commercial MR tri-layer. This material shows a maximum change in resistance of ~1.6%

produce a bias field of ~10 Oe. The samples are deposited such that their anisotropy field is parallel to the bias field of the permanent magnets. This ensures the removal of domain noise.

To test this setup, a commercial MR film was tested. The film consisted of a tri-layer with the following structure: Si/Al_2O_3(1500Å)/β-Ta(50Å)/NiFe(95Å)/β-Ta(50Å). This film was known to have a magnetoresistive ratio between 1.6% and 1.8%. Figure 3.8 shows the measured magnetoresistance of this film. The test apparatus correctly measured the MR ratio of the standard film.

CHAPTER 4: RESULTS

Chapter 4 will present the experimental results obtained from the samples produced by the methods outlined in Chapter 3. The sample annealed for 10 hours, sample AAMMR10, will not be included in this section. Analysis of this sample shows that it suffered contamination during processing. Both the magnetic and magnetoresistive properties of this sample were well outside the trends displayed by the remaining samples. Sample AAMMR10 was produced after the main vacuum chamber was brought up to atmosphere for routine maintenance. The poor properties of this sample were most likely due to contamination of the target surfaces on the sputter sources as well as out-gassing caused during sample heating.

4.1: Vibrating Sample Magnetometer Data

Figures 4.1 and 4.2 shows the result of the magnetometer data for the samples prepared in this study. Several interesting features should be noted. The first important

feature is that the hard and easy axis can be clearly distinguished; the easy axis being induced by the magnetic bias field of 86 Oe during deposition. This feature is important because it allows us to model the hard axis magnetization rotation process that occurs in actual sensor devices. AMR sensors are designed so that the magnetization rotates from the easy axis direction to the hard axis direction. Using the *M-H* loops and the magnetoresistance data, an estimate can be made of the effective anisotropy field, also known as the field needed to saturate the material along its hard axis. It is approximately 20 Oe. This anisotropy field corresponds to the following field-induced anisotropy energy density:

$$K_u \approx \frac{M_s \cdot H_a^{eff}}{2} \approx \frac{10000}{4\pi} \cdot \frac{20}{2} \cdot \frac{erg}{cm^3} \approx 8x10^3 \cdot \frac{erg}{cm^3} \qquad \text{Eq. 4.1}$$

This is reasonably high for the anisotropy energy since bulk Permalloy has an intrinsic magnetocrystalline anisotropy energy of very close to zero at the $Ni_{81}Fe_{19}$ composition.

Another feature to notice in the graphs is the coercivity field, H_c, for each sample. The coercivity increases in the 30-minute annealed sample and then decreases with longer annealing time. The coercivity in all of these films is between 8 Oe and 12 Oe; high quality thin film Permalloy can have a coercivity as low as 1 Oe. There are many factors that control the coercivity of a magnetic material. Dislocations, grain boundaries, and other such defects can act as pinning sites for domain walls. The coercivity can also vary with thickness as one type of domain wall, a Bloch wall, becomes energetically unfavorable and a second type of domain wall, a Néel wall, becomes predominant. At

some critical thickness, both types of domain walls will exist and the coercivity will peak. Impurities in the thin film can also cause an increase in coercivity by either directly changing the chemistry of the material or by acting as pinning sites (if the impurity phase is large enough). Figures 4.1 and 4.2 contain the results of the *M-H* loops for the as-deposited, 30-minute, 3-hour, and 24-hour annealed samples.

4.2: Magnetoresistance Data

Figure 4.3 on page 58 shows the data collected from the *in-situ* four-point probe. The shape of the MR curve correlates nicely to the shape of the *M-H* loops. The bias magnets on the MR probe set the magnetization parallel to the current direction (the high-resistivity state). The bias field also removes the domains in the sample, thereby removing the effect of the coercivity on the MR transfer curve. The coercivity would cause the MR curve to break up into two similar loops offset in the field axis by an amount equal to the coercivity. The maximum slope in the graph, which corresponds to the effective anisotropy field (see chapter 2), occurs, as expected, at ~20 Oe. Saturation of this MR effect occurs around 30 Oe. This is approximately the same field at which the magnetization saturates. While there is an improvement in the maximum magnetoresistance ratio, this ratio only reaches ~1% in the 24-hour annealed sample. Permalloy usually shows a maximum magnetoresistance ratio of 1.5%-2.5% in thin films. The lower than usual MR ratio coupled with the higher than usual coercivity is a possible sign of contamination in the Permalloy element. Looking further at the effects of annealing on the resistivity data can reveal more clues.

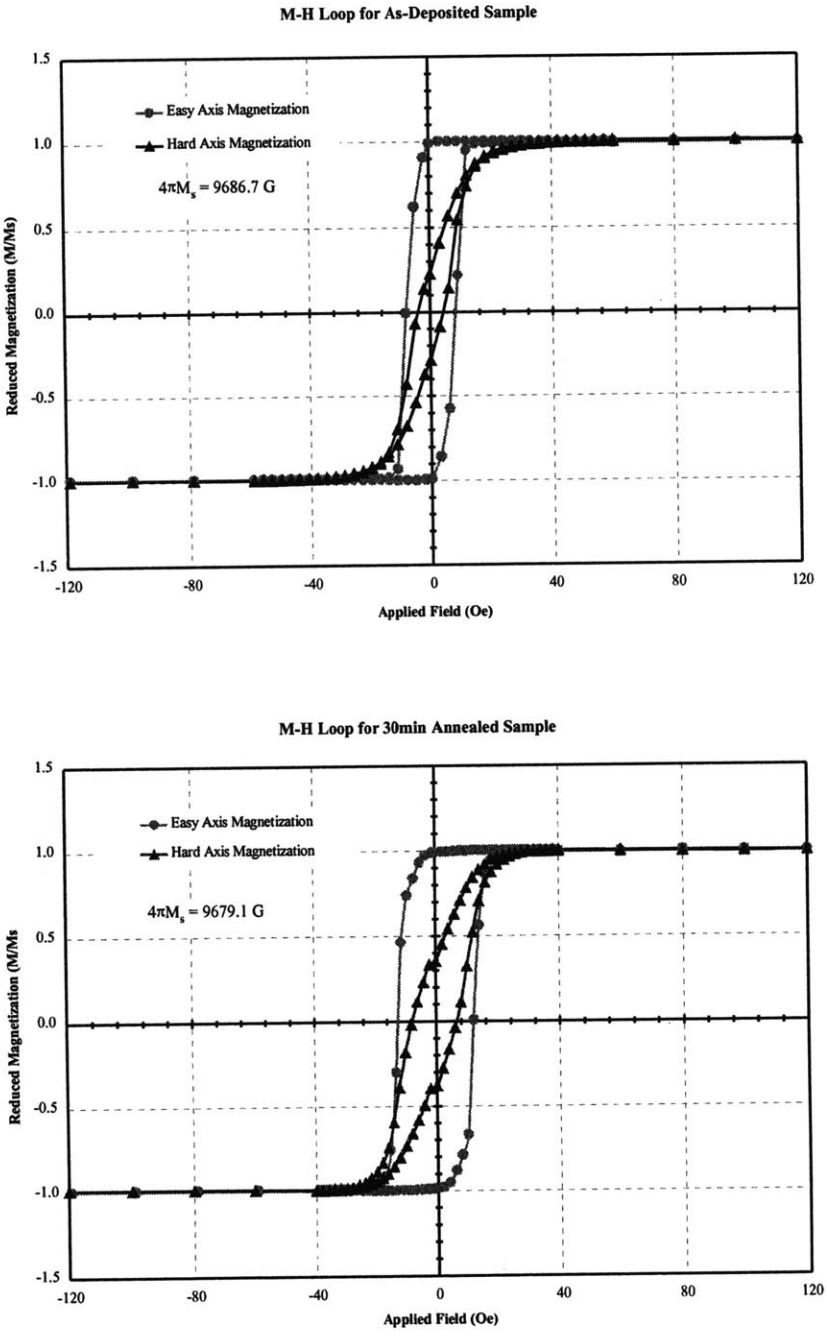

Figure 4.1: M-H loops for the as-deposited and 0.5-hour annealed samples prepared in this study. The samples clearly show the easy axis induced by deposition in a magnetic bias field of 86 Oe. The coercivity is seen to improve with annealing time.

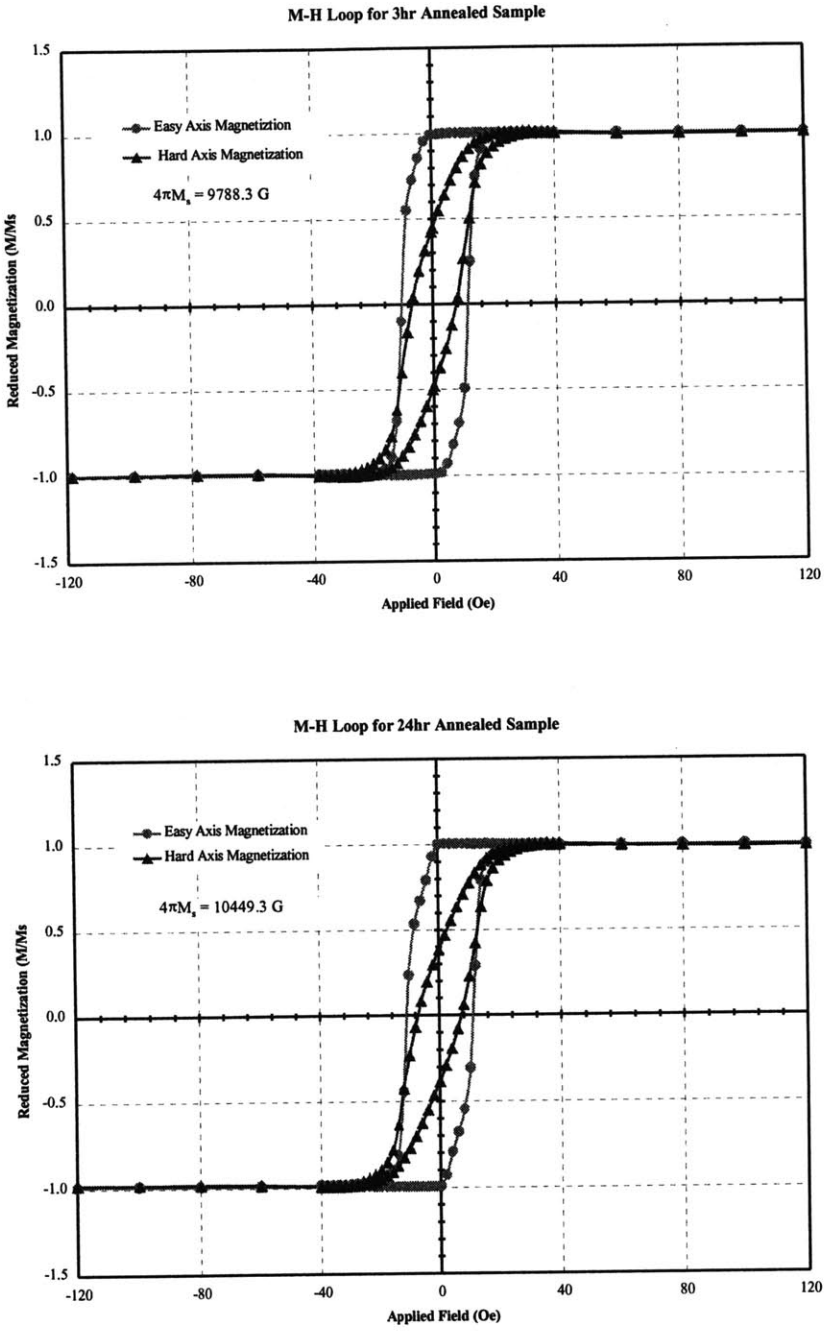

Figure 4.2: M-H loops for the 3-hour and 24-hour annealed samples prepared in this study. The samples clearly show the easy axis induced by deposition in a magnetic bias field of 86 Oe.

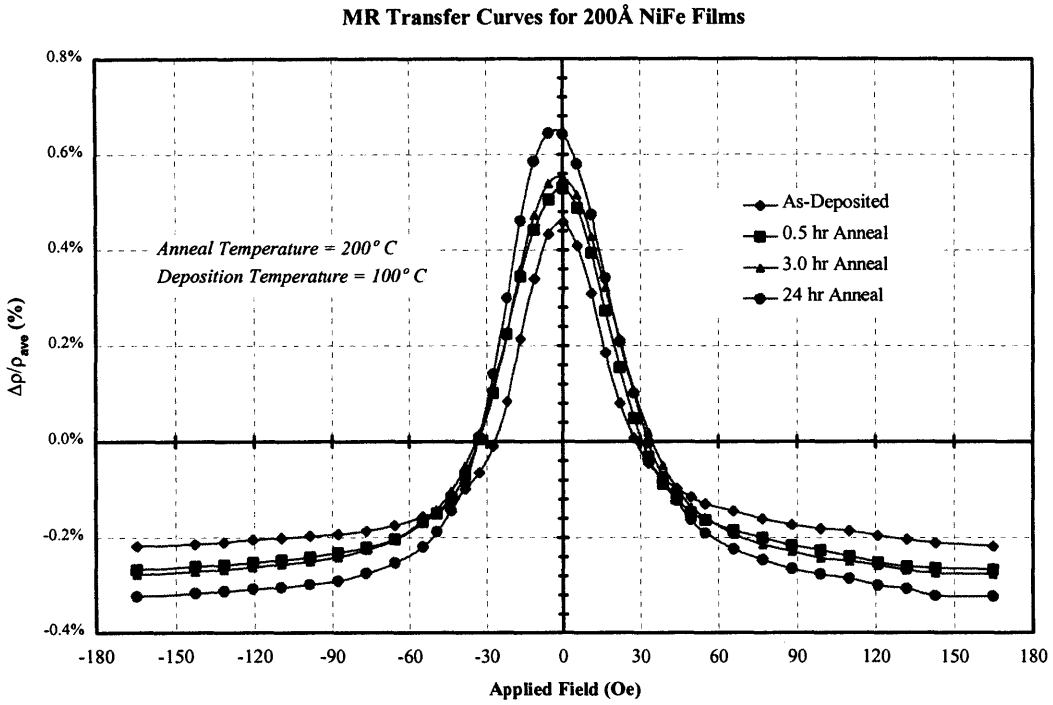

Figure 4.3: Transfer curves for the samples prepared in this study. The MR curves show a distinct improvement between the as-deposited, 0.5-, 3-, and 24-hour annealed samples.

The annealing trends are more clearly illustrated in the graphs of Figures 4.4 and 4.5 on the following pages. These graphs show how annealing affects the maximum magnetoresistance ratio ($\Delta\rho/\rho_{ave}$), the average Permalloy resistivity (ρ_{ave}), the effective anisotropy field (H_a^{eff}), and the maximum field sensitivity. The field sensitivity is the derivative of the MR transfer curve with respect to the applied field. The maximum of this derivative occurs when the magnetization is at an angle of 45 degrees to the current direction; this corresponds to the condition $H_{ext} = H_a^{eff}$. The most significant trend is in the average resistivity data (Figure 4.3(b)). The average Permalloy resistivity is two to three times higher than the bulk resistivity of Permalloy (in a high quality thin film form this would be ~35-40 μΩ-cm).

(a)

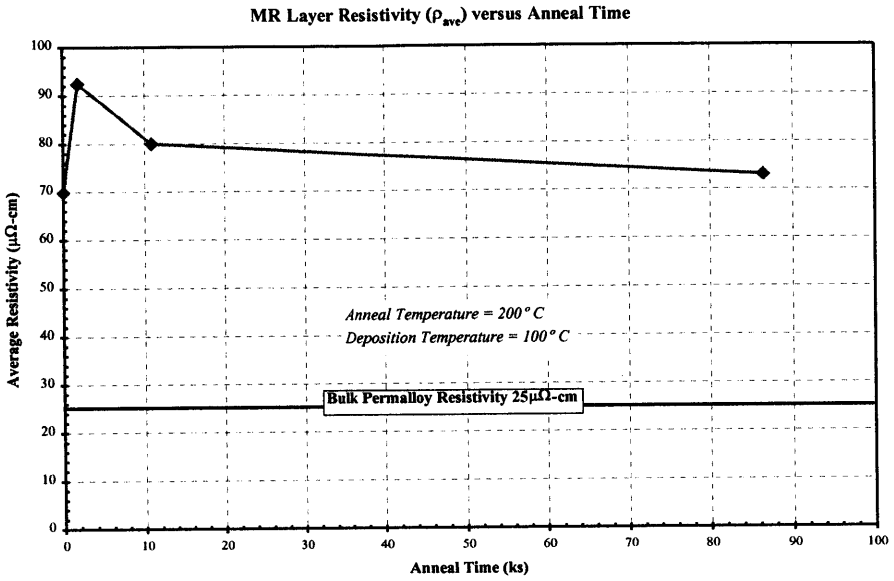

(b)

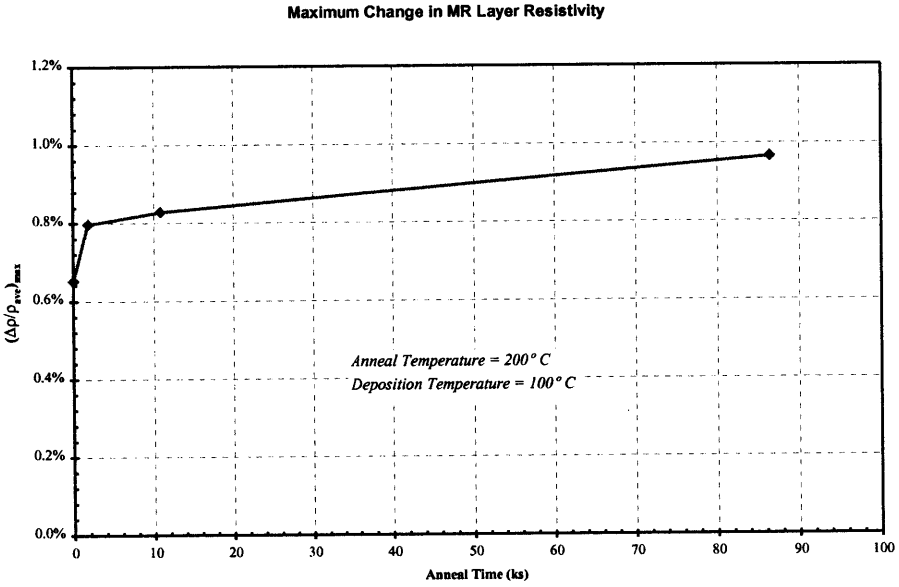

Figure 4.4: These graphs show how various MR properties vary as a function of annealing time. (a) The maximum magnetoresistance ratio and (b) the avearge Permalloy resistivity.

(a)

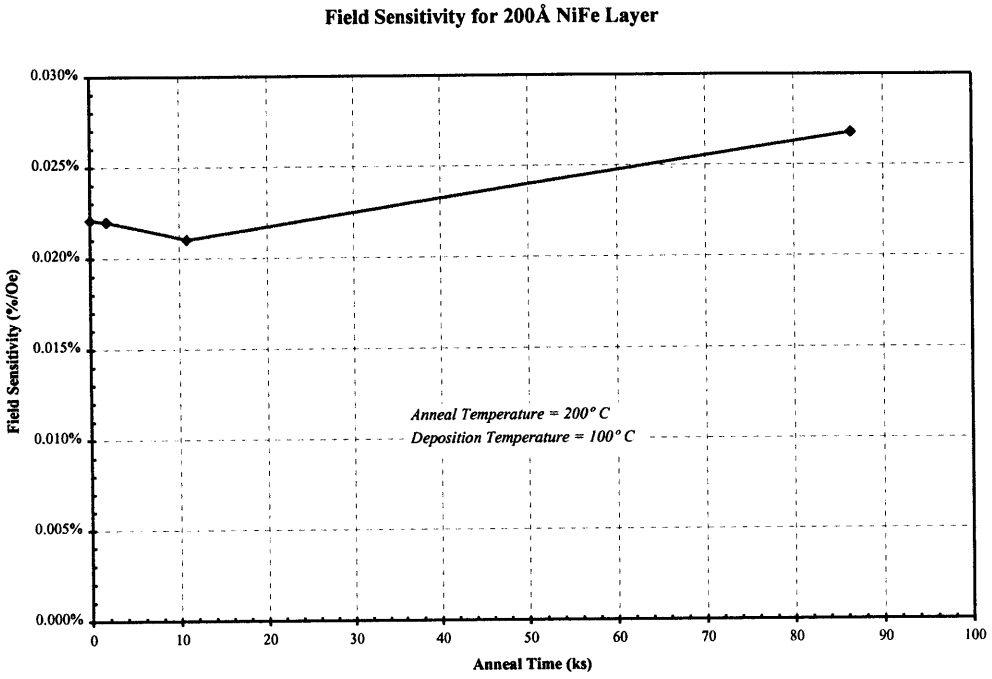

(b)

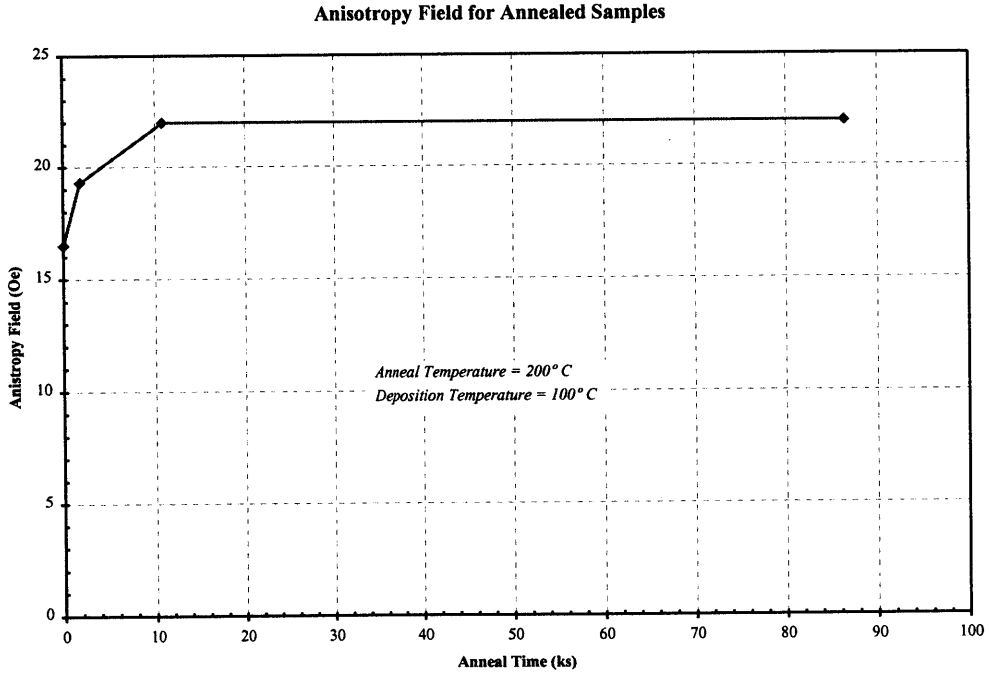

Figure 4.5: These graphs show how various MR properties vary as a function of annealing time. (a) The field sensitivity and (b) the anisotropy field.

The immediate impact of the average resistivity result is that $\Delta\rho/\rho_{ave}$ will be smaller since ρ_{ave} is larger. However, there is still a significant improvement in the maximum $\Delta\rho/\rho_{ave}$ with annealing time between the as-deposited and the 30-minute annealed state. This would suggest that other factors, such as grain structure, are controlling the improved magnetoresistance ratio.

Other improvements can also be seen in the maximum field sensitivity and a stabilization in the effective anisotropy field, H_a^{eff}. The field sensitivity is directly proportional to the $(\Delta\rho/\rho_{ave})_{max}$ and inversely proportional to H_a^{eff}. By improving $(\Delta\rho/\rho_{ave})_{max}$ with annealing, the field sensitivity also improves. A better understanding of what is happening structurally to these films will reveal the role that microstructure might play in this data.

4.3: X-ray Diffraction

Glancing incidence X-ray diffraction (XRD) experiments were performed on each sample to try to determine the orientation of the film and to estimate the grain size. Figure 4.6 shows the (111) peak for these films. It should be noted that the (111) peak was the only resolvable peak in the X-ray diffraction pattern for these films. Because the samples are so thin (total thickness is ~300Å), they produced a very low intensity of diffracted X-rays and only a weak (111) peak can be distinguished from the amorphous background of the glass substrate. The XRD data clearly shows the in-plane orientation of the films to be of a {111} texture. Grain size estimation would require a powder

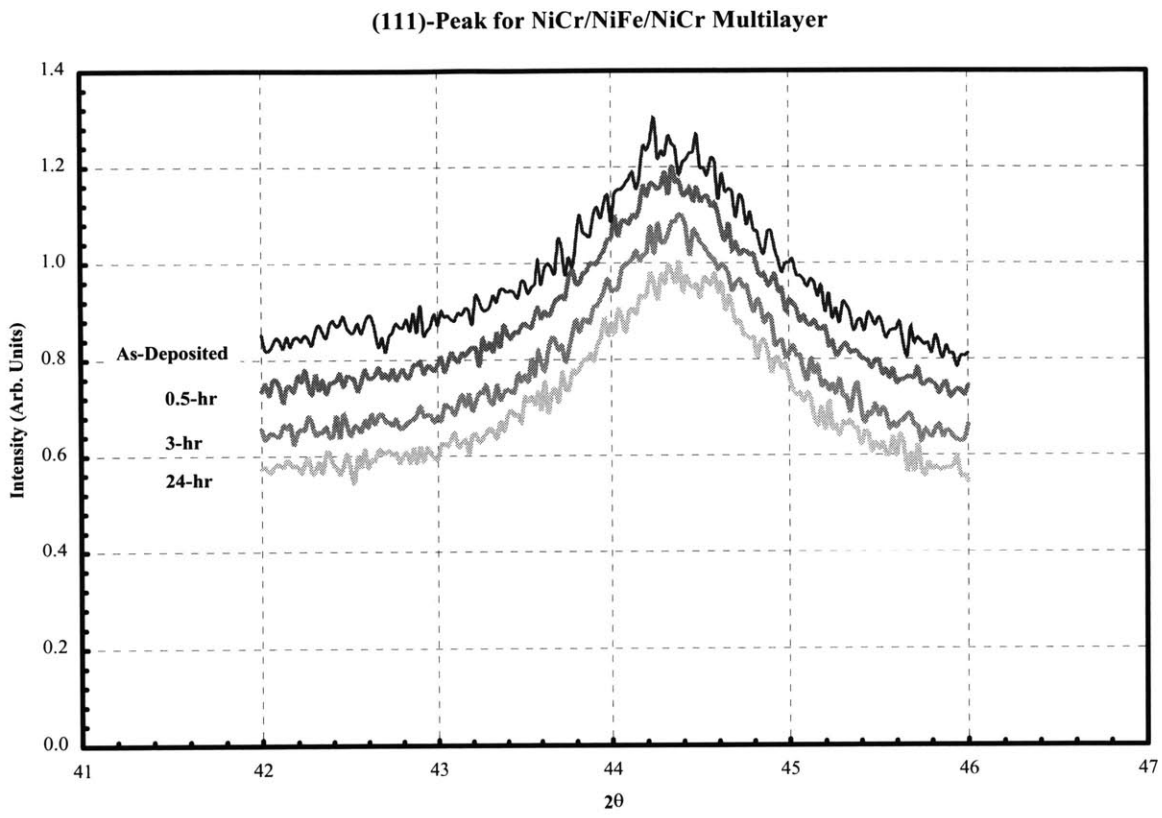

Figure 4.6: The (111) peak for the X-ray diffraction pattern of the annealed NiCr/NiFe/NiCr samples.

sample of known particle size as a reference. Since none were available, an accurate estimation of the grain size could not be made.

4.4: Scanning Electron Micrographs

Scanning electron micrographs (SEM) were taken of the film surfaces after deposition of the final NiFe/NiCr layer. Figure 4.7 shows a 50x and 200x magnifications of the film surfaces for the as-deposited, 3-hour, and 24-hour annealed samples. It is obvious from these images that the surface morphology of the film improves greatly with annealing time. Figure 4.7(a) shows the as-deposited sample. One can clearly make out

the pinholes in the film as well as the roughness of the surface. As annealing progresses, Figures 4.7(b) and 4.7(c), there is a distinct reduction in the pinhole size and density as well as in the surface roughness. Very small pinholes can be seen in the 24-hour annealed sample with 200x magnification (Figure 4.7(c)). This improvement in surface morphology correlates with the improvements seen in the MR data as well as the *M-H* loops for these samples. A discussion of the role of microstructure is found Chapter 5.

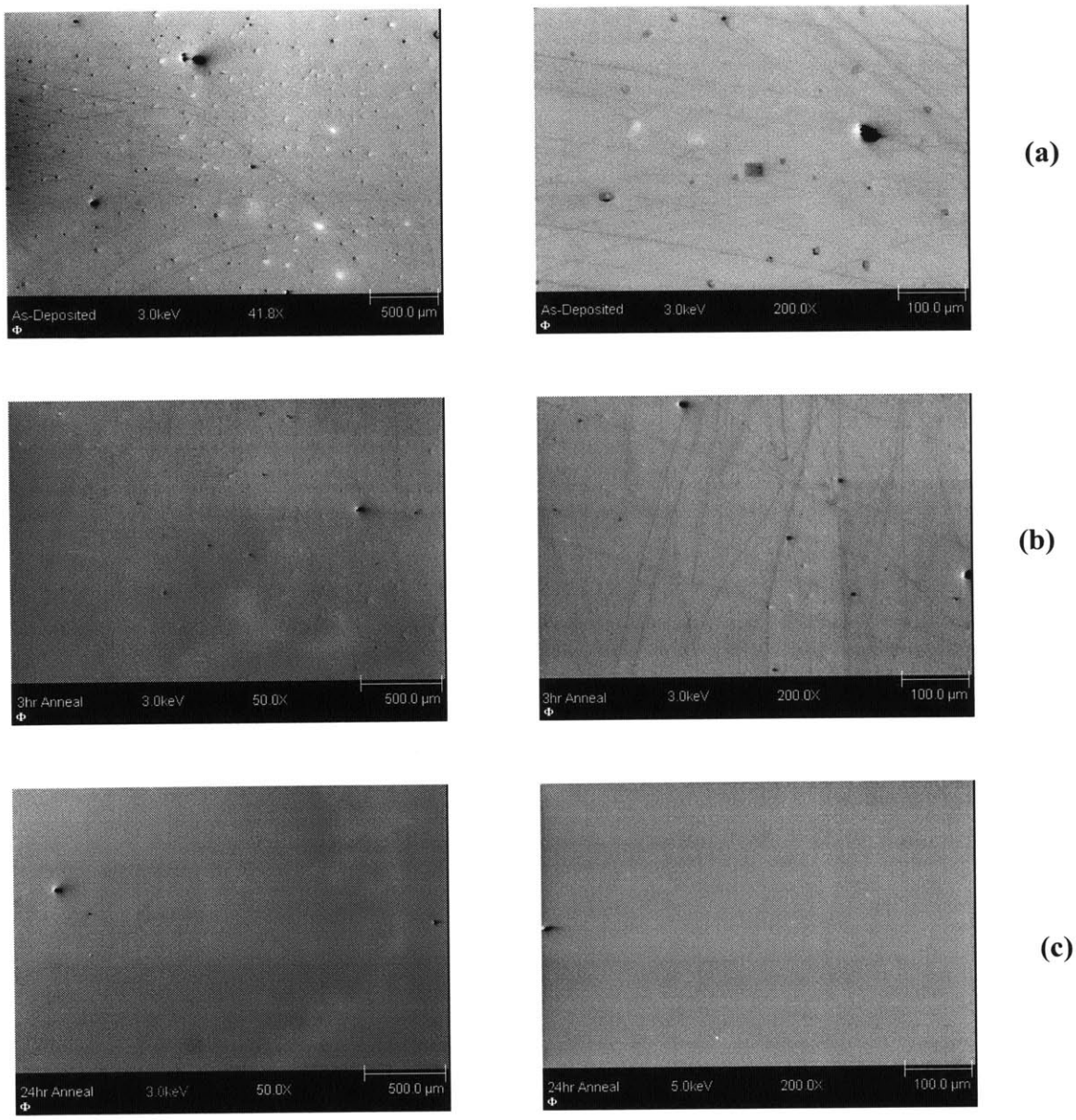

Figure 4.7: SEM images of the surfaces of the thin film multilayers. (a) As-deposited, (b) 3-hour, and (c) 24-hour annealing times. Images on the left are 50x and images on the right are 200x.

CHAPTER 5: DISCUSSION & CONCLUSIONS

The findings of this thesis focus on what roles surface morphology and microstructure play in the magnetoresistive thin films. It is inferred from the data that diffusion of chromium and pinhole development are the factors contributing to trends seen in the MR data as well as the magnetometer data. Section 5.1 will give a brief review of the literature pertinent to this work. Section 5.2 will discuss the specific results of this thesis in light of the literature surveyed in Section 5.1. Finally, the conclusions of this thesis will be given in section 5.3 along with an outline for some future work.

Section 5.1: Literature Survey

Interdiffusion of metallic species in thin film metal couples has been extensively studied, because it is a major source of variation in MR devices at the wafer level as well as in operation[5,34,35]. "Materials intensive" designs of MR devices are the current standard in today's production of thin film magnetic sensors. Devices like spin-valve

GMR sensors and spin-tunnel junction Magnetic-Random Access Memory (MRAM) call for the construction of metallic (and sometimes oxide) multilayers that can be composed of several different levels of transition metal alloys, for example, a SiO_2/FeMn/NiFe/Cu/NiFe/Ta spin-valve. AMR sensors, in particular, call for the construction of a metallic multilayer that has at least four layers of transition metal materials (SiO_2/NiFeCr/β-Ta/NiFe/β-Ta).

One immediate consequence of this "materials intensive" design is the possibility of chemical mixing among these layers. Transition metals have similar chemical properties and can often have very large solubilities with one another. For example, chromium can be dissolved into nickel up to ~50 atomic percent (47 weight percent) as a disordered solid solution. More than 5.6 atomic percent of chromium in nickel will result in complete paramagnetism at room temperature. Tantalum, a 5-d transition metal, has been shown to diffuse rapidly through Permalloy at low temperatures and can form many stable phases with both nickel and iron, for instance, Ni_3Ta. Some systems of transition metals, like Co-Au, are insoluble and will coarsen with annealing but these have not yet been of any technological importance. Hashim *et al.* find that annealing Ta/NiFe multilayers can cause up to a 75% decrease in the saturation moment of the NiFe layer while increasing the coercivity to 8 Oe. Howard *et al.* demonstrate similar results in the FeMn/NiFe/$NiCrO_x$ and FeMn/NiFe/Ta systems used in spin-valves (FeMn is an *antiferromagnet* and is often used as a pinning layer in GMR devices). They report large variations in the coercivity and exchange anisotropy fields due to manganese diffusion via grain boundaries. Coffey *et al.* confirme grain boundary diffusion as the primary

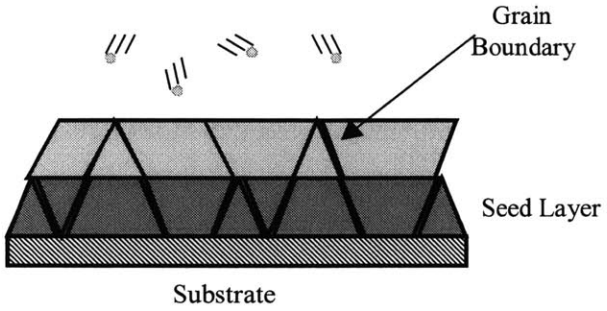

Figure 5.1: A simple depiction of pseudomorphic growth. The growth layer (light gray) extends the crystalline structure of the seed layer (dark gray). Grain boundaries are extended throughout the film structure.

mechanism for the degradation of Ta/Ni thin film couples. It is shown that that the activation energy for grain boundary diffusion in this system is an order of magnitude lower than the bulk diffusion activation energy. These effects present a problem to device designers since the current densities in these devices can be greater than $10^6 A/cm^2$, resulting in operating temperatures in excess of 250°C. To get around such difficulties, device designers have been working on ways of improving heat transfer through the device.

Another important feature of MR devices is that they often use metastable materials; those phases and structures not present on an equilibrium phase diagram. β-Ta, for instance, is a tetragonal, thin film metastable phase of the more common body centered cubic (bcc) Ta, but has a resistivity that is ten times larger than the stable bcc phase ($\rho_{bcc\text{-}Ta}$=20μΩ-cm while $\rho_{\beta\text{-}Ta}$= 200μΩ-cm). Because of this high resistivity, β-Ta works well as a high resistance spacer layer found in AMR sensors. Another example of the use of metastable materials can be found in the construction of spin-valves. $Fe_{50}Mn_{50}$ has been produced in two separate phases. When deposited onto silicon, glass, or quartz, the body-centered cubic α-FeMn phase develops (a=8.81Å). However, when deposited

onto $Ni_{81}Fe_{19}$, the face-centered cubic (fcc) γ-phase is stabilized. It is this latter phase that is technologically important as an *antiferromagnetic* exchange layer. One explanation for this is pseudomorphic growth, that is, grain-to-grain epitaxy (see Figure 5.1)[36,37]. During psuedomorphic growth, an underlying seed layer, like Permalloy, can be used as a template to grow other layers. The expectation is that the grains from the growth layer will grow epitaxially on the grains of the seed layer, thereby transferring their crystal structure and orientation to the growth layer. Transmission electron microscopy observations of the FeMn/NiFe system have shown this to be the case (see reference [36]). Pseudomorphic growth therefore has promise in the area of grain growth and grain boundary reduction. Pseudomorphic growth can be used to reduce the density of grain boundaries in these thin film multilayers, thereby reducing or eliminating one pathway of diffusion. Because NiCr and NiFe have almost identical lattice constants, NiCr can be viewed as potential template material on which to grow NiFe.

Another important feature of these devices is surface morphology. It is important to have high quality, sharp interfaces with very little roughness. Interface integrity is important since device operation depends on the layers being in the same chemical and structural state as when they were deposited. Surface and interface roughness can induce both an in-plane magnetic anisotropy and ferromagnetic coupling between layers. Pinholes in thin films are a consequence of many factors during film growth, such as surface and interface energies, strain energy, etc. These film defects need to be eliminated in devices since they can give rise to ferromagnetic coupling or electrical shorting between layers. Many authors have studied the stability of interfaces and

thermodynamics of grain and pinhole growth in thin films[38,39,40,41]. Depending on the interface and strain energies involved, the details of the materials used, and the heat treatment process, many types of film texture and structure can be developed. In all of these thermodynamic and kinetic treatments of grain and hole growth, film thickness and temperature are the controlling factors.

5.2: Discussion of Data

In Chapter 4, several important features appear in the data collected from the annealed samples:

1. Annealing the substrate prior to deposition of the magnetoresistive layer improved the maximum magnetoresistance ratio, that is, $(\Delta\rho/\rho_{ave})_{max}$ increases with increasing t_{anneal}.

2. The average resistivity of the magnetoresistive layer decreased with longer annealing times, that is, ρ_{ave} decreases as t_{anneal} increases.

3. The average resistivity of the magnetoresistive layer was 2 to 3 times larger than the bulk value of Permalloy (~25μΩ-cm).

4. The maximum magnetoresistance ratio was 50–70% of that expected for a Permalloy thin film (~1% for NiCr/NiFe/NiCr versus 1.6% to 2.5% for β-Ta/NiFe/β-Ta).

5. The coercivity of the MR element was 8 to 12 times larger then the coercivity of bulk Permalloy (~1Oe).

6. The effective anisotropy field increased and then stabilized with longer annealing times.

7. X-ray diffraction showed a {111} in-plane texture in all films.

8. SEM micrographs showed a lower surface roughness and pinhole density with longer annealing times.

There are two possible ways to explain the lower than usual $(\Delta\rho/\rho_{ave})_{max}$ and the larger than usual ρ_{ave}. First, the low value of $(\Delta\rho/\rho_{ave})_{max}$ might be due to the increase in the average resistance of the Permalloy layer, ρ_{ave}. This increase in resistivity could be associated with the reduced grain size, increased roughness, and surface scattering due to decreasing the film thickness. These surface scattering effects are collectively called the *size effect*. Using the Sondheimer-Fuchs theory[42,43] of diffuse scattering, one can show that:

$$\rho \approx \rho_o \cdot \left[1 + \frac{3}{8} \cdot \left(\frac{l_0}{t}\right)\right] \qquad \text{Eq. 5.1}$$

In Equation 5.1, l_o is the mean free path of electrons, ρ_o is the bulk resistivity of the material, and t is the thickness of the film. Using a value of 25μΩ-cm for ρ_o, 150Å for l_o[44], and a film thickness of 200Å, the resistivity would be ~32μΩ-cm. The resistivities that are measured in these experiments are still 2.5 times larger than this value!

A more plausible explanation of this increase in resistivity would be to assume that chromium has diffused into the Permalloy layer. We may justify this assumption by noting that Permalloy can remain ferromagnetic with up to several atomic percent of chromium dissolved in it. For instance, Cr-Permalloy (3.8Cr-78Ni-18.2Fe) has a saturation moment ($4\pi M_s$) of ~8000G, a coercivity of 4Oe and a resistivity of 60μΩ-

cm[45]. Using equation 5.1 and a value of 60μΩ-cm for the bulk resistivity, the resistivity of a 200Å Cr-Permalloy layer would be ~77μΩ-cm. This value for the resistivity is very close to what has been experimentally measured in the samples. Chromium additions to a nickel host are also known to significantly reduce the MR ratio[46,47]. The theory of chromium diffusion is also supported by the fact that the Permalloy layer was deposited at 100°C and under a -200V electrical bias. The high deposition temperature as well as the large kinetic energy of impinging gas atoms could be responsible for significant mixing of chromium into the Permalloy layer.

While the above argument can be used to explain the poor MR properties of the samples, the improvement with seed layer annealing time still has yet to be explained. As mentioned previously, lattice-matched polycrystalline thin film materials exhibit pseudomorphic growth during deposition. A review of the available powder diffraction data shows that both $Ni_{80}Cr_{20}$ and $Ni_{81}Fe_{19}$ have similar lattice constants ($a \approx 3.54$Å). By depositing and annealing the NiCr seed layer at a high temperature (T_s = 200°C), higher surface mobility is imparted to the arriving atoms. Coupling this high temperature to a low growth rate allows the columnar grain structure inherent in sputtered films to coalesce. Void density decreases and the films become more continuous. Thompson *et al.* (1985 & 1993) have developed extensive theories for the growth of grains in thin films and the evolution of thin film texture. Here is a brief highlight of some of the main points:

1. The thermodynamic driving force for grain growth is $\Delta F \propto -1/t_{film}$.

2. The radius of a growing grain is proportional to the growth time. In other words, the longer the sample is annealed, the larger its grain size.

3. Grain growth occurs at a faster rate in thinner films.

4. Texture development is a sensitive function of film thickness and deposition temperature. A global minimum in the surface free energy of fcc metals is found in the {111} planes. A {111} texture will develop in very thin fcc metal films.

When the Permalloy layer is deposited, it mimics the underlying grain structure of the seed layer. Because the NiCr seed layer is so thin (~50Å), there is a large driving force for coalescence. This improvement in film structure could also explain the decrease in resistivity with longer annealing times. The {111} texture of the films is caused by the driving force to minimize the surface energy. {111}-planes have the lowest surface energy for fcc NiCr and NiFe.

SEM micrographs also support the view of improved surface morphology in the annealed films. This improvement in film microstructure can explain the improvements seen in the maximum MR ratio. From the micrographs, it is apparent that the surface roughness and pinhole density decreases with annealing time. A high deposition temperature along with a long annealing time allows for higher adatom mobility in the plane of the growing surface. This high adatom mobility would allow the growing surface to coalesce or 'wet' the substrate. Srolovitz *et al.* have shown that the critical radius for pinhole growth and shrinkage is proportional to the film thickness and that the details of the growth and shrinkage depends upon the surface free energy of the materials

involved and the state of stress in the film. With very little data on the surface energies in this film/substrate system, it is hard to estimate the driving forces involved. For fcc metals, surface energies are on the order of 10^3 erg/cm^2 (mJ/m^2). Since the annealing temperature is low, the strain energy developed from thermal expansion differences ($\alpha_{glass} \approx 0.5$ ppm/°C and $\alpha_{Ni} \approx 12$ ppm/°C) would certainly be lower than the surface energies involved. Thus, the reduction in the pinhole density seen in the SEM images could imply that the NiCr wets the glass surface in order to minimize the surface energy of the system. This argument is also made plausible by the fact that chromium will react with SiO_2 glass, breaking Si-O bonds, to form Cr-O and Cr-Si bonds[24].

5.3: Conclusions & Future Work

This thesis presents a study of SiO_2/NiCr/NiFe/NiCr for use in AMR sensor applications. A number of important features were outlined that have implications not only for AMR devices, but also for spin-valve and other layered magnetic structures. The data clearly shows an improvement in the surface morphology of the thin film multilayer, which leads to improved magnetoresistive properties. Pseudomorphic growth of grains was cited as an explanation for this effect. An annealing treatment of the seed layer prior to deposition of the MR layer led to a lower resistivity of the MR layer, a lower coercivity, and a larger maximum MR ratio and field sensitivity. While diffusion of chromium and pinholes could be a problem in these films, a modification of deposition conditions could be implemented to optimize the microstructure of these films and minimize diffusion.

In order to understand the role processing parameters play in the NiCr/NiFe/NiCr system, these same experiments should be performed at lower electrical bias and lower deposition temperatures. Doing so would allow for the elimination of chromium diffusion. Also, a diffusion study of chromium through NiFe would be useful in determining how active grain boundary diffusion is in this system. Finally, it would be interesting to anneal a NiCr/NiFe/NiCr multilayer at various temperatures and measure the changes in magnetoresistance as a function of annealing time and temperature. This last test would result in an understanding of the thermal limitations of this system.

BIBLIOGRAPHY

1) Prinz, Gary A., *Science*, **282**, 1660 (27 November 1998)

2) Fontana, Robert E., *et al.*, J. Appl. Phys., **81**, 3998 (1997)

3) J.G. Holl-Pellerin, S.G.H. Anderson, P.S. Ho, K.R. Coffey, J.K. Howard, K. Barmak, *Mat. Res. Symp. Proc.*, Vol. 313, 205 (1993)

4) M.H. Tabacniks, A.J. Kellock, J.E.E. Baglin, K.R. Coffey, J.K. Howard, M.A. Parker, *Mat. Res. Symp. Proc.*, Vol. 382, 389 (1995)

5) I. Hashim, H.A. Atwater, K.T.Y. Kung, R.M. Valletta, *Mat. Res. Symp. Proc.*, Vol. 232, 159 (1991)

6) D. E. Thompson *et al.*, IEEE Trans. Magn. **11**, 1039 (1975)

7) P. Baumgart, B.A. Gurney, D. Wilhoit, T. Nguyen, B. Dieny, V.S. Speriosu, J. Appl. Phys. **69**, 4792 (1991).

8) B. Dieny, V.S. Speriosu, S. Metin, S.S.P. Parkin, B.A. Gurney, P. Baumgart, D.R. Wilhoit, J. Appl. Phys. 69, 4774 (1991).

9) Peter Singer, "Read/Write Heads: The MR Revolution," Semiconductor International, vol. 2, 1997, pp. 71.

10) W. Thomson, Proc. Roy. Soc., vol. 8, pp. 546-550, 1857.

11) J. L. Snoek, Nature, vol. 163, pp. 837-838, 1949.

12) J. Smit, Physica, vol. XVI, No. 6, pp. 612-627, June 1951.

13) H. C. van Elst, Physica vol. 25, pp. 708-720, 1959.

14) J. Craik, *Magnetism: Principles and Applications*, John Wiley and Sons, New York, 1996.

15) E. C. Stoner, Proc. R. Soc. London, Ser. A **165**, 372 (1938)

16) J. E. Hirsch, Phys. Rev. B **40**, 2354 (1989); **40**, 9061 (1989); **43**, 705 (1991); Physica B **163**, 291 (1990); Phys. Rev. B **59**, 6256 (1999).

17) M. B. Stearns, Physics Today, April 1978; J. Appl. Phys. **72**, 5354 (1992); Mat. Res. Soc. Symp. Proc. vol 313, pp 553.

18) N. F. Mott, Proc. Roy. Soc. **153**, 699 (1936), Proc. Roy. Soc. **156**, 368 (1936), Adv. in Phys. **13**, 325 (1964), see also A. Fert and I. A. Campbell, J. Phys. F **6**, 849 (1976).

19) R. R. Birss, *Symmetry and Magnetism*, North-Holland Press, Amsterdam, 1964.

20) C. M. Hurd, Adv. Phys. **23**, 315 (1974).

21) R. M. Bozorth, *Ferromagnetic Materials*, John Wiley and Sons, New York, 1965; R. M. Bozorth, *Ferromagnetism*, van Nostrand and Co., 1954, IEEE Press, 1993. J.A. Osborn, Phys. Rev. **67**, 351, 1945.

22) R. P. Hunt, IEEE Trans. **MAG-7**, 150 (1971)

23) Thompson *et al.*, IEEE Trans. **MAG-11**, 1039 (1975)

24) For a description of thin film deposition techniques, see D. L. Smith, *Thin Film Deposition: Principles & Practice*, McGraw Hill, New York 1995

25) M Ohring, *The Materials Science of Thin Film*, Academic Press, Boston 1992, pp. 129-131.

26) B. D. Cullity, *Elements of X-ray Diffraction* 2nd edition, Addison-Wesley, Reading, MA 1978.

27) L. J. van der Pauw, Philips Research Reports, vol. 13, 1 (1958).

28) Uhlir, Bell Systems Technical Journal, vol. 34, 105 (1955).

29) F. M. Smits, Bell Systems Technical Journal, vol. 37, 711 (1958).

30) L. B. Valdes, Proc. I.R.E., vol. 42, 420 (1954).

31) J. Shi and Y. Sun, Rev. Sci. Instrum., **68** 1814 (1997).

32) R. H. Norton, IEEE Trans. Magn., **MAG-19**, 1579 (1983).

33) C. Hwang et al., MRS Symp Proc **232**, 217 (1991).

34) M. H. Tabacniks et al., MRS Symp Proc **382**, 389 (1995).

35) C. Hwang *et al.*, JAP **64**, 6116 (1988).

36) C. Hwang *et al.*, MRS Symp Proc **232**, 211 (1991).

37) C. V. Thompson, JAP **58**, 763 (1985).

38) C. V. Thompson, Scripta Met Mat **28**, 167 (1993).

39) C. V. Thompson *et al.*, MRS Symp Proc **403**, 63 (1996).

40) D. J. Srolovitz, MRS Symp Proc **403**, 3 (1996).

41) K. Fuchs, Proc. Cambridge Phil. Soc., vol. 34 pp. 100 (1938).

42) E. H. Sondheimer, Adv. In Phys., vol. 1, pp. 1 (1956).

43) T. R. McGuire, IEEE MAG-11, 1018 (1975).

44) S. Chikazumi and S. Charap, *Physics of Magnetism*, John Wiley and Sons, New York 1964, pp.494.

45) P. Muth *et al.*, Phys. Stat. Sol., vol. 126 k69 (1991).

46) P. Muth *et al.*, J. Phys. F, vol. 11 pp. 2119 (1981).